Materials Advances

ROYAL SOCIETY OF CHEMISTRY

PAPER

View Article Online
View Journal | View Issue

Cite this: *Mater. Adv.*, 2026, 7, 3885

Rheology and coaxial extrusion of acellular and cell-laden hollow conduits of pristine kappa carrageenan and gold–kappa carrageenan nanocomposite hydrogels

Sanchari Swarupa,[a] Mata Subhashita,[b] Nikita Chauhan,[c] Jitendra Bahadur,[cd] Sharad Gupta[a] and Prachi Thareja*[be]

Received 19th February 2026,
Accepted 2nd March 2026

DOI: 10.1039/d6ma00245e

rsc.li/materials-advances

This study explores the use of kappa carrageenan (κCG) hydrogels to create cell-laden hollow conduits *via* multi-material extrusion with a coaxial nozzle. We used an in-house setup with two syringe pumps to extrude both ionically crosslinked κCG and gold–κCG nanocomposite (κCG–AuNP) hydrogels for the conduit shell and a sacrificial core into a crosslinking bath. We tested various κCG compositions and flow rates, finding that the inner filament diameters ranged from 625 to 700 μm and the outer diameters from 1000 to 1030 μm. Perfusion assays showed that 2% (w/v) κCG–AuNP hydrogels extruded at higher flow rates maintained integrity, allowing for uniform perfusion in longer filaments. Rheological analysis indicated that gold nanoparticles (AuNPs) reduced both the storage moduli and the viscosity of the hydrogels, and the crosslinking bath improved storage moduli post-crosslinking. The 2% (w/v) κCG–AuNP hydrogels demonstrated delayed breakage during high-flow rate extrusion, facilitating handling during perfusion. Importantly, the addition of A549 cells did not impact the rheological properties or pinch-off dynamics, and cell viability exceeding 60% was noted within the conduit walls. Thus, the 2% (w/v) κCG–AuNP hydrogel shows promise for rapid fabrication of hollow conduits for *in vitro* modelling of tubular biological structures.

1. Introduction

The overarching goal of tissue engineering is to fabricate scaffolds that recapitulate the complex microarchitecture of native tissues to be functional. This includes designing vascular artificial tissues that can mass transport fluids like blood, oxygen, and nutrients, similarly to physiological tissues.[1] Coaxial extrusion is a one-step strategy for creating hollow or multi-material tubular constructs by extruding two distinct biopolymers simultaneously through a coaxial nozzle.[2] Extrusion can either be pneumatic or piston-facilitated. Piston extrusions are generally achieved using syringe pumps.[3] One of the commonly employed methods for the fabrication of artificial vascular conduits is the multi-material extrusion of a cross-linkable hydrogel along with a sacrificial core that can be dissolved or removed by physical methods.[4] There is a rapidly growing interest in using Pluronic F-127, a synthetic biopolymer, as a sacrificial core in coaxial extrusion. Its excellent printability, shear-thinning behaviour, and sol-like characteristics at 4 °C make Pluronic F-127 ideal for creating easily tunable hollow channels with varying inner lumen diameters. This can be achieved by adjusting the compositions of the shell biopolymer ink and their flow rates.[5]

The existing literature on coaxial extrusion focuses on alginate as the preferred biomaterial for fabricating hollow tubes, owing to its excellent mechanical properties and rapid ionic crosslinking using $CaCl_2$.[6–8] Kappa carrageenan (κCG), like alginate, is an anionic polysaccharide composed of alternating galactose and 3,6-anhydrogalactose units. It has recently been repurposed from a food additive to the biomedical field by modifying it to form hydrogels, fibres, scaffolds, *etc.*, due to its biocompatibility, biodegradability, and thermoresponsive gelling capacity.[9] κCG has been previously explored for both 3D printing and bioprinting by our group and by Marques and colleagues, respectively, who demonstrated high cell viability and reorganisation in 3D-printed scaffolds.[10,11] Previous work from our group has also demonstrated the fabrication of κCG

[a] *Department of Biological Sciences and Engineering, IIT Gandhinagar, Palaj, Gujarat 382355, India*
[b] *Department of Chemical Engineering, IIT Gandhinagar, Palaj, Gujarat 382355, India. E-mail: prachi@iitgn.ac.in*
[c] *Solid State Physics Division, Bhabha Atomic Research Centre, Mumbai, 400085, India*
[d] *Homi Bhabha National Institute, Anushaktinagar, Mumbai, 400094, India*
[e] *Dr. Kiran C. Patel Centre for Sustainable Development, IIT Gandhinagar, Palaj, Gujarat 382355, India*

hydrogel beads and emulsion gels.[12,13] However, there is a paucity of information on fabricating κCG-based hollow perfusable conduits. Therefore, based on the existing literature on κCG and alginate, we hypothesize that since κCG is also a negatively charged biopolymer similar to alginate, capable of crosslinking with positively charged ions, it should also be able to form self-supporting hollow tubes when crosslinked with potassium chloride (KCl). Although κCG can also be ionically crosslinked with Ca^{2+}, different ions induce different gelation behaviours in κCG. K^+ ions are known to form stronger gels of κCG compared to Na^+ or Ca^{2+} ions.[14] In contrast, Ca^{2+} ions yield κCG gels of lower stiffness, reducing the elastic modulus with increasing Ca^{2+} concentration.[15] Moreover, Lim and colleagues have reported no toxicity on NIH 3T3 cells in methacrylated κCG hydrogels crosslinked with K^+ ions during extrusion from a coaxial nozzle for the fabrication of cell-laden scaffolds.[16] This precedent established KCl as a safe ionic crosslinker for the fabrication of cell-laden hollow fibers.

Nevertheless, it is important to note that the mechanism of ionic crosslinking and gelation differs between alginate and κCG. The κCG hydrogel undergoes crosslinking in the presence of counterions *via* helix aggregation driven by ionic interactions. Monovalent cations like K^+ neutralize the negatively charged sulphate groups on their polymeric chains, inducing helical secondary structure formation, resulting in gelation.[17,18] In contrast, alginate undergoes ionic interactions with Ca^{2+}, forming an egg-box-like structure that ultimately leads to dimer formation. These dimers further undergo multimerization, leading to gelation.[19] It is important to emphasize that the main objective of this study is not to prove that the κCG hydrogel is superior to alginate. Instead, the goal is to investigate whether this relatively underexplored biopolymer can be optimised as a suitable material for coaxial extrusion, capable of supporting living cells during and after the extrusion process.

In addition to the above, κCG, as a sulfated polysaccharide, can function as a polyelectrolyte, self-assembling during nanoparticle formation and providing stability to the nanoparticles within their soft matrices.[20] Previous reports have shown that the pendant hydroxyl groups of κCG can be a capping and stabilizing agent for metallic nanoparticles.[21,22] Metallic gold nanoparticles (AuNPs) in polymer matrices confer additional biological and mechanical properties. Depending on their shape and size, AuNPs can promote cell adherence in scaffolds, induce cell differentiation and maturation, improve cell–cell coupling by imparting electrical conductivity to the scaffold system, and modulate scaffold's mechanical properties.[23] The presence of AuNPs in hydrogels can increase the stiffness of soft natural biopolymer-based matrices such as GelMA while simultaneously improving the shear thinning behaviour, making these nanocomposite hydrogels ideal for optimal cell attachment, adhesion, and bioprinting.[24] There are also many reports on *in situ* synthesized gold-chitosan nanocomposite hydrogels as candidates for biomedical applications, including tissue engineering and drug delivery.[25,26]

κCG has also been used as a reducing and stabilising agent for AuNPs, for instance, in the degradation of azo dyes.[21] There have been limited studies on gold–κCG nanocomposites exploring their biomedical applications, including antitumor activity and wound-healing properties.[27–29] Notably, a previous report utilised low concentrations of κCG, ranging from 0.5 mg mL^{-1} to 0.08 mg mL^{-1}, to synthesize AuNPs but was unable to form hydrogels. The study found that AuNPs in κCG did not induce significant cytotoxicity in the A549 lung cancer cell line. The AuNPs could also quench reactive oxygen species (ROS), exhibiting antioxidative behaviour.[30] Thus, the formation of *in situ* AuNPs and their impact on cell viability in a true hydrogel matrix comprising a higher concentration of κCG, suitable for extrusion and formation of self-supporting hollow tubes, have not been addressed. Rheological analysis of a κCG and locust bean gum composite hydrogel with *in situ* synthesized AuNPs revealed a decrease in viscosity with an increase in the concentration of $HAuCl_4$ added to κCG, thereby imparting superior shear thinning properties.[31] However, efforts remain limited in exploring gold-κCG nanocomposite hydrogels for bioink printability, rheological characterization, cell-laden 3D-printed constructs, and vascular constructs. We envision that AuNPs in κCG hydrogels will modulate their rheological behaviour, enhance cell viability in a 3D microenvironment, and potentially improve the biological properties of the hollow conduits.

During coaxial extrusion, the material mainly experiences shear flow within the nozzle. Once the material exits the nozzle, it transitions to extensional flow as it is deposited onto the build surface. Therefore, understanding the extensional properties of complex fluids is essential not only for processing operations, such as jetting, spinning, and coating, where extensional modes of deformation are dominant, but also for analysing bio-inks used in extrusion and printing. Materials often exhibit significantly different behaviours in extensional flow compared to shear flow.[32] Devices like the Capillary Breakup Extensional Rheometer (CaBER) provide valuable insights by observing the thinning and breaking of a fluid filament.[33] In polymer solutions, extensional flows can cause flexible macromolecules to uncoil, resulting in either extensional thinning or thickening. This phenomenon significantly alters the fluid's flow response.[34] Slight variations in factors such as molecular weight, structure, temperature, and concentration can affect how a sample reacts under extension, making extensional rheological characterization a valuable tool for quality control. While traditional methods like CaBER are commonly used, alternative techniques, such as the dripping-on-substrate method, can also provide extensional characterization. This method involves slowly dispensing the sample from a nozzle onto a substrate surface to form a liquid bridge, which creates a filament that eventually breaks due to capillary forces.[35] Using a high-speed camera to record this process yields valuable data on the fluid's extensional properties, providing a practical and informative approach to rheological analysis.

A previous work from our lab demonstrated successful printing of complex shapes using 1% (w/v) κCG crosslinked

with 25 mM KCl, achieving excellent biocompatibility (98%) of A549 lung cancer epithelial cells seeded on the hydrogel surface after 24 hours.[36] Previous work conducted by Sasikumar C. and group utilised lung epithelial cells, such as L-132 and A549, to prepare bioinks of mucin and hyaluronic acid for 3D bioprinting with the aim of fabricating printed lung tissues. Notably, κCG-based hydrogels with *in situ* synthesized AuNPs having an average particle size of 14.3 ± 2.1 nm were reported to exhibit no cytotoxicity on A549 cells.[30] A549 cells have also been widely used for 3D bioprinting to fabricate cell-laden porous grid scaffolds as lung cancer models.[37,38]

However, to date, no report has employed A549 cells to coaxially bioprint hollow tubular structures as potential lung cancer models. Therefore, in this study, we demonstrate the fabrication of hollow tubular conduits from an acellular gold–κCG (κCG–AuNP) nanocomposite, pristine κCG, and A549 lung carcinoma cells encapsulated in both κCG–AuNP and κCG hydrogels. This was achieved using coaxial extrusion followed by ionic crosslinking in a post-extrusion bath, utilising a sacrificial core of Pluronic F-127. We monitored changes in channel diameters as a function of the flow rates of the sheath κCG and κCG–AuNP hydrogel inks and the uniform formation of hollow conduits, using microscopic imaging and perfusion assays. Rheological investigations and pinch-off dynamics results indicated that both the weight percentage (wt%) of κCG and the presence of AuNPs significantly influenced the storage modulus, viscosity, and filament breakage time of the inks. Additionally, we studied the effects of encapsulating lung carcinoma cells at a concentration of 2×10^6 cells per mL in κCG and κCG–AuNP hydrogels on their rheological properties and pinch-off dynamics. Our findings suggest that the presence of AuNPs did not introduce additional toxicity into the encapsulated lung carcinoma cells, enabling the successful formation of biocompatible, cell-laden κCG–AuNP hydrogel hollow conduits.

2. Materials and methods

2.1. Sample preparation

To prepare a pristine κCG crosslinked hydrogel, 150 mg, 200 mg, and 225 mg of kappa carrageenan powder (Sigma-Aldrich) were mixed with 10 mL of 10 mM potassium chloride (KCl). This yielded hydrogels with different concentrations of κCG: 15 mg mL^{-1} (1.5% w/v), 20 mg mL^{-1} (2% w/v), and 22.5 mg mL^{-1} (2.25% w/v), respectively. The mixture was stirred in a water bath maintained at 70 °C at 800 rpm for 2 hours, until the κCG powder was completely dissolved. The pristine κCG inks will be referred to as 1.5κCG, 2κCG, and 2.25κCG throughout the manuscript.

To *in situ* synthesize AuNPs in κCG hydrogels, 150 mg, 200 mg, and 225 mg of κCG powder were dissolved in 10 mL of a 10 mM potassium chloride (KCl) solution. This preparation yielded hydrogels with different concentrations of κCG: 15 mg mL^{-1} (1.5% w/v), 20 mg mL^{-1} (2% w/v), and 22.5 mg mL^{-1} (2.25% w/v), respectively. The aqueous mixture was heated to 70 °C in a water bath while continuously stirring at 800 rpm. Once the water bath reached 70 °C, 1 mL of a 1.52 mM gold(III) chloride trihydrate ($HAuCl_4 \cdot 3H_2O$) solution (Sigma-Aldrich) was added to the mixture, which was then stirred for 24 hours. From this point onward, the *in situ* synthesized gold–κCG nanocomposite inks will be referred to as 1.5κCG–AuNP, 2κCG–AuNP, and 2.25κCG–AuNP throughout the manuscript.

2.2. Characterization of *in situ* synthesized AuNPs in κCG hydrogels

The synthesis of AuNPs within hydrogel matrices containing different weight percentages of κCG was confirmed through UV-visible spectrophotometry after a 24-hour reaction period. The size of the AuNPs was evaluated using atomic force microscopy (AFM). Samples were prepared as described previously and diluted to 1 mg mL^{-1} before drop-casting onto mica sheets. The prepared slides were allowed to dry in a desiccator for 24 hours before AFM imaging (Bruker NanoWizard Sense) in tapping mode. Nanoscope analysis software was utilised to process and analyse the images obtained. The hydrodynamic size of the AuNPs was also determined by dynamic light scattering (DLS) using a Brookhaven NanoBrook instrument. Similar to AFM, the samples were first diluted to 1 mg mL^{-1} in filtered deionized water before measurement.

The functional groups in κCG–AuNP and κCG hydrogels were further characterized by Fourier transform infrared (FTIR) spectroscopy using a Bruker Invenio-S FTIR spectrometer. The ATR probe was pressed directly onto the lyophilized samples placed on the crystal stage and scanned over the spectral range of 400–4000 cm^{-1}.

2.3. Coaxial extrusion

A pre-built coaxial nozzle from Rame-Hart Instrument Co. (USA) was used, consisting of an inner needle with an inner diameter (I.D.) of 584 μm (20G) and an outer needle with an inner diameter of 1190 μm (16G). This nozzle was connected to two 5 mL syringes: one containing a 30% (w/v) solution of Pluronic F-127 and the other containing either pristine κCG or κCG–AuNPs, as illustrated in Fig. 1. The samples were loaded into the syringe barrel while pristine κCG and κCG–AuNPs were

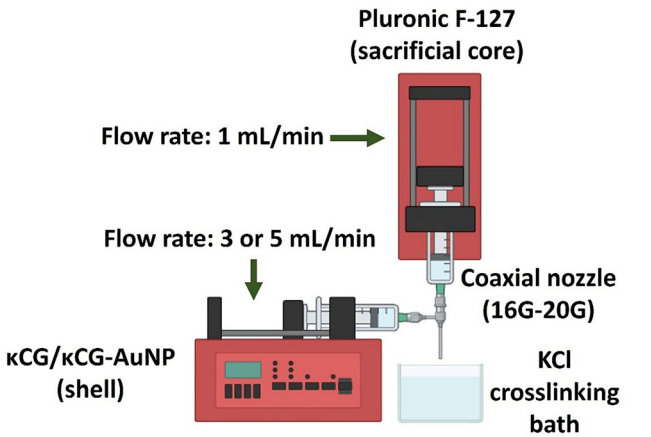

Fig. 1 Coaxial extrusion set-up. Figure created using Biorender.com.

in a sol state at elevated temperatures. This was followed by an incubation time of 10–12 minutes, during which the hydrogel temperature was allowed to decrease to 37 °C, with continuous monitoring by a temperature probe. The extrusion was initiated only after the hydrogel attained a temperature of 37 °C.

Pluronic F-127 was extruded through the inner needle using a syringe pump to create the core of the filaments at a fixed flow rate of 1 mL min^{-1}. Simultaneously, pristine κCG or κCG–AuNP hydrogels were extruded through the outer needle using a syringe pump at different flow rates of 0.5–5 mL min^{-1}, immediately after 37 °C was attained. The extruded filaments were deposited directly into a Petri dish containing 100 mM KCl solution, which served as a post-extrusion crosslinking bath (see the Supplementary Movie). The nozzle was positioned 4–5 mm above the crosslinking bath. The filaments immersed in the crosslinking bath were incubated at 4 °C for half an hour to remove the sacrificial core of Pluronic F-127. After incubation, the 100 mM KCl solution was discarded, and the cross-sections of the hollow filaments were imaged using a stereomicroscope. The circularity index of the lumens of the hollow channels was determined using the following equation:

$$c = \frac{4\pi A}{L^2} \quad (1)$$

where c is the circularity index, A is the cross-sectional area, and L is the perimeter of the hollow lumen. A perfect circle has a circularity index of 1; an elongated shape has a circularity index of 0.[39]

2.4. Perfusion assay

The consistency of hollow channel fabrication after coaxial extrusion was evaluated using a perfusion assay. A green food dye was injected through the hollow lumen of the filaments using a 5 mL syringe equipped with either a 23G nozzle (inner diameter = 330 μm) or a 27G nozzle (inner diameter = 200 μm).

2.5. Rheology

The rheological properties of the hydrogels forming the shell of the hollow filaments were evaluated 24 hours after preparation using a stress-controlled modular compact rheometer (Anton Paar MCR302). All rheological measurements of the pristine κCG and κCG–AuNP hydrogels were performed at an extrusion temperature of 37 °C. The samples were equilibrated at 37 °C for 10 minutes before conducting any rheological tests.

The rheological characterization of the bath-crosslinked pristine κCG and κCG–AuNP hydrogels was conducted at 25 °C on the same day as sample preparation. This involved casting and punching out hydrogel discs with a thickness of 2 mm and a diameter of 25 mm, which were then incubated in a 100 mM KCl bath at 4 °C for half an hour.

To determine the linear viscoelastic region (LVR) of both κCG and κCG–AuNP hydrogels, a large amplitude oscillatory strain sweep was performed, ranging from 0.01% to 1200% strain at a constant angular frequency of 6.28 rad s^{-1}. The dynamic viscoelastic moduli were measured *via* a small-amplitude oscillatory frequency sweep spanning 0 to 100 rad s^{-1} at a fixed strain within the LVR region. Additionally, the phase angle was determined from the frequency sweeps using the following equation:

$$\tan\delta = \frac{G''}{G'} \quad (2)$$

where G'' is the loss modulus and G' is the storage modulus.

The flow curves of the hydrogels were obtained by increasing the shear rate logarithmically from 0.01 to 100 s^{-1} to analyse their flow behaviour. The power law model was used to characterize the shear-thinning properties of the hydrogels. The values of n and K were calculated from the shear rate–viscosity curves by fitting them to the following power law equation:

$$\eta = K\dot{\gamma}^{n-1} \quad (3)$$

where η is the viscosity and $\dot{\gamma}$ is the shear rate.

The experiments were conducted using a parallel plate geometry with a diameter of 50 mm and a gap of 0.5 mm. The bath-crosslinked hydrogel discs were tested using a parallel plate with a diameter of 25 mm and a gap of 2 mm.

2.6. Mechanical characterization

The mechanical properties of the hydrogels forming the shell material of the hollow filaments were quantified using a universal testing machine (UTM) under unconfined compression. Pristine κ-carrageenan (κCG) and κCG–AuNP hydrogels were tested in the as-prepared state and after ionic crosslinking by immersion in a 100 mM KCl bath at 4 °C for 30 min. Cylindrical specimens (n = 3 per condition; height ≈ 16 mm, diameter ≈ 15 mm) were placed centrally on a 70 mm compression plate and compressed using a parallel 70 mm upper plate at a crosshead speed of 1 mm min^{-1} until failure (see the Supplementary Movie). Engineering stress–strain curves were calculated from the recorded force–displacement data, and the compressive modulus was determined from the slope of the initial linear region of the stress–strain response.

2.7. Filament pinch-off dynamics experiments

A dripping-onto-substrate rheometry setup was constructed in the lab to measure the pinch-off dynamics and extensional properties of κCG and κCG–AuNP hydrogels at 37 °C. A glass slide was mounted horizontally, positioned 10 mm below a vertical syringe. The syringe was connected to a syringe pump, which extruded samples at flow rates of 3 mL min^{-1} and 5 mL min^{-1}, consistent with the rates used during coaxial extrusion, until the sample touched the substrate and formed a hydrogel filament. The pumping was then switched off.

An LED light source and a high-speed camera operating at 5000 frames per second recorded the thinning of the filament diameter ($D(t)$) over time. These videos were analyzed using a custom MATLAB code to track the evolution of the filament diameter ($D(t)$) with each frame. Up to 10 trials were conducted to ensure repeatability, and the average decay profiles of the filament diameter ($D(t)$) were used for further analysis.

Surface tension (σ) measurements of the κCG and κCG–AuNP hydrogels were crucial for analysing extensional

parameters. These measurements were performed using the method proposed by Adrian Daerr, as other methods, such as tensiometer measurements, posed challenges and proved unreliable for hydrogels.[40]

The rheological characterization of complex fluids often requires determining a constitutive parameter known as the characteristic relaxation time (λ). This parameter quantifies the amount of elastic energy present in the sample. Eqn (4) describes the exponential decay of $D(t)$, providing valuable insights where λ is the characteristic extensional relaxation time, t is the observation time, and D_o is the internal diameter of the Luer lock of the syringe barrel (1880 μm). When stress is applied in an extensional mode, the viscosity coefficient is referred to as extensional viscosity (η_e). The extensional strain rate is derived from the filament diameter and its rate of change over time, as shown in eqn (6) and (7).[41–43]

$$\frac{D(t)}{D_o} = \left[e^{-t/3\lambda}\right] \quad (4)$$

$$\frac{d(D(t))}{dt} = \frac{D(t)_n - D(t)_{n-1}}{(t)_n - (t)_{n-1}} \quad (5)$$

$$\dot{\varepsilon} = \frac{-2}{D(t)} \times \frac{d(D(t))}{dt} \quad (6)$$

$$\eta_e = \frac{-\sigma}{\frac{d(D(t))}{dt}} \quad (7)$$

2.8. Cell culture and cell-laden coaxial extrusion

Lung carcinoma cells (A549) were cultured at 37 °C and 5% CO_2 in Dulbecco's Modified Eagle Medium (DMEM) (Gibco), supplemented with 10% fetal bovine serum (FBS) and 1% penicillin–streptomycin. For cell-laden coaxial extrusion, the same setup was used under sterile conditions. The cells were trypsinized with 0.25% Trypsin-EDTA (Gibco) and suspended at a concentration of 2×10^6 cells per mL in pristine κCG and κCG–AuNP hydrogels. The flow rate of the cell-laden κCG and κCG–AuNP hydrogels was maintained at 5 mL min^{-1}, and they were deposited in a confocal dish containing a crosslinking bath of 100 mM KCl.

After post-extrusion crosslinking in 100 mM KCl at 4 °C, the filaments were washed with 1× phosphate-buffered saline (PBS) and incubated in complete DMEM media at 37 °C for 24 hours. The extrusion process was carried out inside a laminar flow cabinet, and both the shell and sacrificial core hydrogel samples were prepared using autoclaved deionized water (DI) under sterile conditions. Additionally, the coaxial nozzle was autoclaved for half an hour before the cell-laden coaxial extrusion experiments.

2.9. Cell viability assay

After incubating the cell-laden hollow filaments in cell culture media at 37 °C for 24 hours, a live–dead assay was conducted to assess the viability of the seeded A549 cells. The filaments were first washed with a 1× PBS buffer following the gentle removal of the media. Calcein AM (2.25 μM) and propidium iodide (3.75 μM) were diluted in serum-free media to prepare the staining solution. Next, 1 mL of this staining solution was gently added to the confocal dish containing the hollow filaments and incubated at 37 °C for 15 minutes. Three representative images were captured using a Leica TCS SP8 confocal microscope at 10× magnification. The cell viability was calculated using:

$$\text{Viability} = \frac{\text{Live cells}}{\text{Live} + \text{Dead cells}} \times 100\% \quad (8)$$

3. Results and discussion

3.1. Characterization of AuNPs

The successful synthesis of gold AuNPs within the polymer matrices of κCG hydrogel was investigated using spectrophotometric analysis, as shown in Fig. 2(a). The maximum absorption values observed – approximately 532 nm, 534 nm, and 531 nm for 1.5κCG–AuNP, 2κCG–AuNP, and 2.25κCG–AuNP, respectively – confirm the reduction of Au^{3+} to Au^0 by the hydroxyl groups of κCG chains. Additionally, a visible color change from a transparent κCG solution to pink was noted during the formation of AuNPs, attributed to the surface plasmon resonance (SPR) phenomenon.

The characteristic peaks obtained from the height profiles of Fig. 2(b)–(d) show that the AuNPs synthesized within the κCG matrix appear to be mainly spherical, along with the presence of aggregates that result in some irregular shapes. Also, the UV visible absorption spectra of all κCG–AuNP compositions are all approximately close to 540 nm, which is the standard absorption wavelength of spherical AuNPs (Fig. 2(a)).[44] According to Belloti *et al.*, when using AFM to measure the diameter of spherical AuNPs, the most accurate method of determining the diameter is by measuring the height (z-axis) obtained from the cross-section profiles, rather than the x–y lateral dimensions. This is primarily because the AFM tip has a finite shape and size, which may lead to a broadening effect known as tip dilation. This phenomenon causes the nanoparticles to appear wider than their true diameter in the x–y plane. In contrast, the height or z-axis remains unaffected by the shape and size of the tip, making the height measurements of the cross-section profiles a more reliable approach to measure AuNP diameters.[45] Hence, following the above approach, we considered the true diameter of spherical AuNPs to be the top height obtained from the cross-section profiles, thereby avoiding any error caused by tip dilation. The average height of the AuNPs obtained from the images ranged from 10 to 35 nm. SAXS analysis of κCG–AuNP hydrogels further supported the AFM results, indicating that the AuNPs were well-dispersed within the gel network, with an average diameter of 15–16 nm across the different κCG compositions (Fig. S3(c)).

The absorption peak is significantly influenced by the size and shape of the formed nanoparticles.[46] The presence of AuNP aggregates, or an increase in their size, has been shown to cause a shift or broadening of the maximum absorption peak.[47]

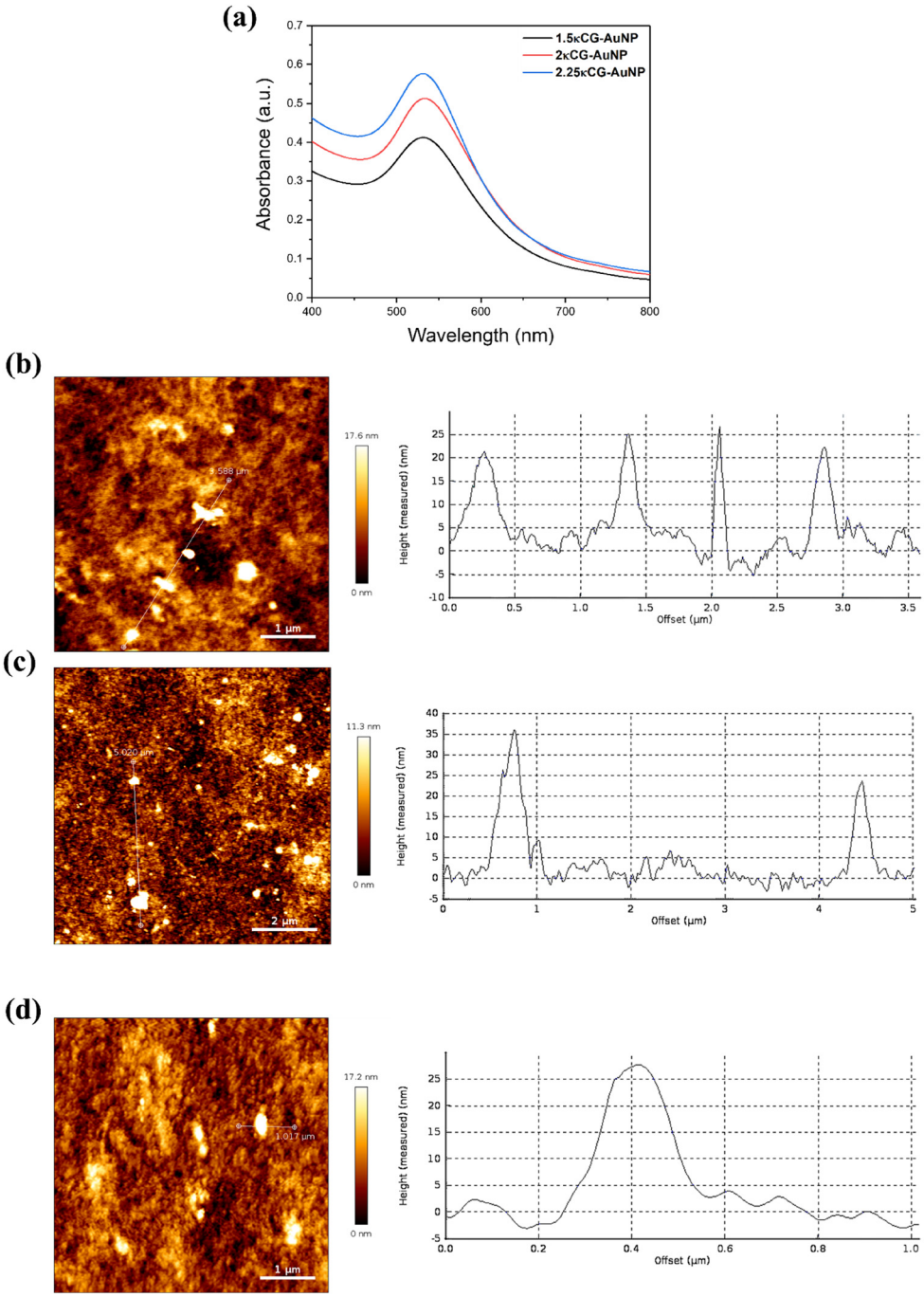

Fig. 2 (a) UV-visible spectra of AuNPs synthesized in various compositions of κCG for 24 hours in a water bath at 70 °C; (b), (c) and (d) AFM image and height profiles of 1.5κCG–AuNP, 2κCG–AuNP and 2.25κCG–AuNP hydrogels, respectively.

As illustrated in Fig. 2(a), all three compositions of κCG–AuNP hydrogels display similar absorption peaks and maxima. Therefore, it is likely that the shape and size of the AuNPs synthesized in these three different κCG–AuNP hydrogel compositions are also similar, as confirmed by the cross-section height profiles shown in Fig. 2(b)–(d).

Moreover, the number-weighted size distribution profiles obtained by DLS also confirm that the hydrodynamic diameter of the *in situ* synthesized AuNPs is similar across all κCG compositions (Fig. S1). The average hydrodynamic diameter of all κCG–AuNP compositions is approximately 758 nm. It is known that the light scattering intensity is proportional to the sixth power of particle radius, due to which DLS is more sensitive to bigger particles.[48] Hence, we have reported the number-weighted size distribution of AuNPs in κCG. The size derived from DLS was found to be larger than that observed by AFM, since the AuNPs are associated with their respective κCG polymer compositions in the swollen state, resulting in complex shapes and increased roughness. Furthermore, various interactions like H-bonding, van der Waals and π–π

interactions may lead to larger coordination spheres of polymer-capped AuNPs.[21] The intensities of the maximum absorption peaks for the three compositions of the κCG–AuNP hydrogels in Fig. 2(a) suggest that the amount of AuNPs synthesized within the hydrogels increases with a higher weight percentage of κCG.

Wan *et al.* previously synthesized *in situ* AuNPs in a solution containing 18 mg mL^{-1} (1.8% w/v) κCG. The optimal reaction conditions included a temperature of 80 °C, a reaction time of 30 minutes, and a concentration of 0.4 mM $HAuCl_4$. Transmission electron microscopy (TEM) analyses revealed that the mean size of the nanoparticles ranged from 13.5 nm to 18.6 nm.[21] Álvarez-Viñas and colleagues demonstrated the creation of larger, pseudo-spherical nanoparticles (ranging from 14 nm to 36 nm) in a 0.25 mg mL^{-1} (0.025% w/v) carrageenan solution, as the concentration of chloroauric acid increased.[49] In addition, Débora A. de Almeida *et al.* synthesized κCG-capped AuNPs with a hydrodynamic size of 563 ± 7 nm.[50] It is well-documented that the shape and size of AuNPs formed *in situ* depend on the reaction conditions; however, the size range of the AuNPs obtained in our samples aligns with the existing literature. Since the size range of AuNPs synthesized remained in the same range irrespective of the concentration of κCG explored, any difference in rheological and mechanical properties due to variation in size of AuNPs will not be apparent, allowing us to isolate the concentration of κCG as the primary driver of the mechanical stability of the hollow tubes.

The *in situ* synthesis of AuNPs was further confirmed by the subtle shifts in the characteristic O–H stretching bands compared to the pristine κCG hydrogels in the FTIR spectra of all compositions of lyophilized κCG hydrogels (Fig. S2). All the compositions of κCG–AuNP hydrogels displayed a shift of the –O–H stretching band by 2–12 cm^{-1} compared to the O–H bands of the pristine κCG hydrogels. These shifts likely arise from the involvement of hydroxyl groups in coordinating Au^{3+} ions, thereby contributing to the nucleation and stabilization of AuNPs within the κCG matrix.[51] Concomitantly, the perturbation of the O–H stretching region suggests a partial disruption of intermolecular hydrogen bonding between κCG chains, likely resulting from competitive interactions of κCG hydroxyl groups with the AuNP surface. Secondary bands show characteristic features of κCG at 2904–2910 cm^{-1}, 1636–1640 cm^{-1}, 1372–1374 cm^{-1}, 1224–1227 cm^{-1}, 1035–1036 cm^{-1}, 918–922 cm^{-1}, 842–844 cm^{-1} and 698–700 cm^{-1} corresponding to C–H stretching, bound water vibration, CH_2 in plane bending, S–O stretching, glycosidic linkage, C–O–C stretching of 3,6-anhydro-D-galactose, and O–S–O symmetric vibration of sulfate esters and sulfate on C-4 galactose, respectively.[51,52] The absence of significant changes in these bands indicates that the primary polysaccharide backbone of κCG remains structurally intact following AuNP incorporation.

3.2. Coaxial extrusion

To identify the optimal flow rates for achieving uniform extrusion from a coaxial nozzle, extrudability tests were performed on various compositions of pristine κCG and κCG–AuNP hydrogels, using flow rates ranging from 0.5 to 5 mL min^{-1}. As shown in Fig. 3(a), a flow rate of 0.5 mL min^{-1} was insufficient to extrude any of the compositions from the coaxial nozzle. At 1 mL min^{-1}, extrusion was not possible for the highest weight percentages of both pristine κCG and κCG–AuNP hydrogels, and only droplet formation was observed for the 2κCG and 2κCG–AuNP compositions. Uniform extrusion at 1 mL min^{-1} was achieved only for the lowest compositions of 1.5κCG and 1.5κCG-AuNP; however, frequent filament breakage occurred during the initial stages. At flow rates of 2, 2.5, and 3 mL min^{-1}, filament breakage was a common issue across all compositions except for 1.5κCG, which exhibited uniform extrusion with minimal breakage at the beginning. At the highest flow rate of 5 mL min^{-1}, all compositions successfully achieved uniform extrusion with the least frequency of breakage, resulting in the production of continuous, longer filaments.

Based on the above analysis, 3 mL min^{-1} and 5 mL min^{-1} were selected for further studies, since continuous extrusion was observed for all compositions only at these two flow rates. Flow rates exceeding 5 mL min^{-1} were not tested, keeping in mind the potential negative impacts of high shear rates on encapsulated cells.

The morphology of the κCG–AuNP and pristine κCG filaments extruded at two selected flow rates after incubation in a 100 mM KCl bath is shown in Fig. 3(b and c). The cylindrical nature of the hollow tubes is clearly visible. Longer filaments (>50 cm) were attained using the higher flow rate of 5 mL min^{-1} for both κCG–AuNP and pristine κCG hydrogels. The dimensions of coaxial-extruded hollow channels were evaluated by imaging the cross-sections using a stereomicroscope (Fig. 4(a and b)). The cross-sectional images of the filaments made from 2κCG, 2.25κCG, 2κCG–AuNP, and 2.25κCG–AuNP hydrogels showed hollow conduits, confirming the complete removal of the sacrificial core made of Pluronic F-127 at flow rates of 3 mL min^{-1} and 5 mL min^{-1}. Additionally, we conducted coaxial extrusion of 1.5κCG–AuNP and 1.5κCG hydrogels, as indicated in Fig. S4. The filaments produced from both the 1.5κCG–AuNP and 1.5κCG hydrogels exhibited collapsed lumens or ruptured cross-sections (Fig. S4).

The dimensions of the inner channel diameter, outer diameter, and wall thickness are generally known to depend on the flow rate of the sheath biopolymer. Previous research has indicated that increasing the speed of the sheath results in an increase in the outer diameter of hollow fibers.[3,53] Fig. 4(c and d) illustrate the impact of the flow rate of κCG through the outer nozzle on the hollow lumen diameter, outer diameter, and wall thickness. Increasing the flow rate from 3 mL min^{-1} to 5 mL min^{-1} significantly enlarged the wall thickness of 2κCG–AuNPs. However, other than the above, no significant differences in inner diameter, outer diameter, or wall thickness were observed in the 2.25κCG–AuNP or pristine 2κCG and 2.25κCG hydrogel filaments. To assess the reproducibility of dimensions of hollow conduits using the setup, we performed 5 independent extrusion experiments and subsequently quantified the dimensions of 15 cross-sections by imaging under a

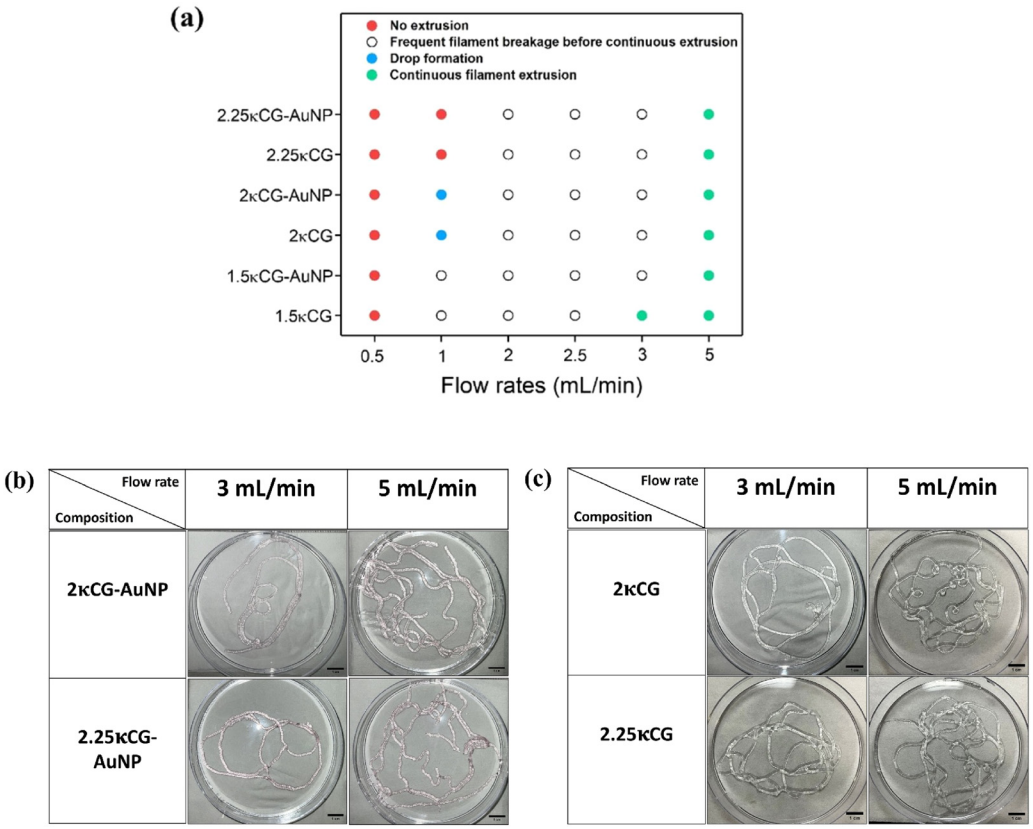

Fig. 3 (a) Extrudability map of varying compositions of pristine κCG and κCG–AuNP hydrogels extruded out of a pre-built coaxial nozzle (16G-20G); (b) and (c) images of extruded filaments after incubation in a KCl bath (scale bar: 1 cm).

stereomicroscope. The mean values and standard deviations for I.D., O.D., wall thickness and circularity of the hollow channels are presented in Table 1, while the coefficients of variation (CV) are reported in Table 2. According to the literature, a CV $\leq$ 30% is considered acceptable across experiments.[54] As shown in Table 2, all measured parameters exhibited CVs below this threshold, indicating that the extrusion process yielded constructs with satisfactory reproducibility and dimensional consistency.

The circularity index ranging between 0.82 and 0.92 in Table 1 indicates that the cross-sections of the extruded filaments were closer to a perfect circle (with a circularity index of 1) rather than an elongated shape (with a circularity index of 0). Therefore, all compositions of κCG and κCG–AuNP hydrogels, extruded at different flow rates, were able to form circular self-supporting hollow lumens after the removal of Pluronic F-127 from the core by incubation in a 100 mM KCl bath at 4 °C for 30 minutes.

3.3. Perfusability

A dye injection test was conducted to evaluate the formation of a uniform hollow channel in the extruded tubular structures after the removal of the sacrificial core, to determine their perfusability (Fig. 5 and the accompanying Movie in the SI). Perfusion was only successful for shorter filaments, measuring between 2 and 3 cm when extruded at a flow rate of 3 mL min^{-1} for all compositions of κCG and κCG–AuNPs. Additionally, there was a higher incidence of breakage during the manual handling of these shorter filaments.

In contrast, a continuous flow of dye was observed in longer filaments, greater than 5 cm, which were extruded at a flow rate of 5 mL min^{-1} across all compositions of κCG and κCG–AuNPs. Among these, the longest filaments made from 2κCG–AuNPs were the most successful and could be handled without breakage during the perfusion assay, as illustrated in Fig. 5.

To gain a better understanding of how the concentration of κCG, the influence of AuNPs, the effects of the ionic crosslinking bath, and the extrusion flow rate contribute to the successful formation of filaments with a self-supporting hollow lumen, we characterized the hydrogels using both rotational and extensional rheology, as detailed in the following sections.

3.4. Rheological studies

A complete rheological characterization of the pristine κCG and κCG–AuNP hydrogels was performed to capture their viscoelastic and shear flow behaviours under conditions relevant to extrusion and post-extrusion crosslinking (Fig. 6). Small amplitude oscillatory frequency sweep (SAOS) experiments were conducted on pristine κCG and κCG–AuNP hydrogels at an extrusion temperature of 37 °C. Large amplitude oscillatory strain sweeps (LAOS) for all ink compositions were used to determine the linear viscoelastic region (LVR), as illustrated in

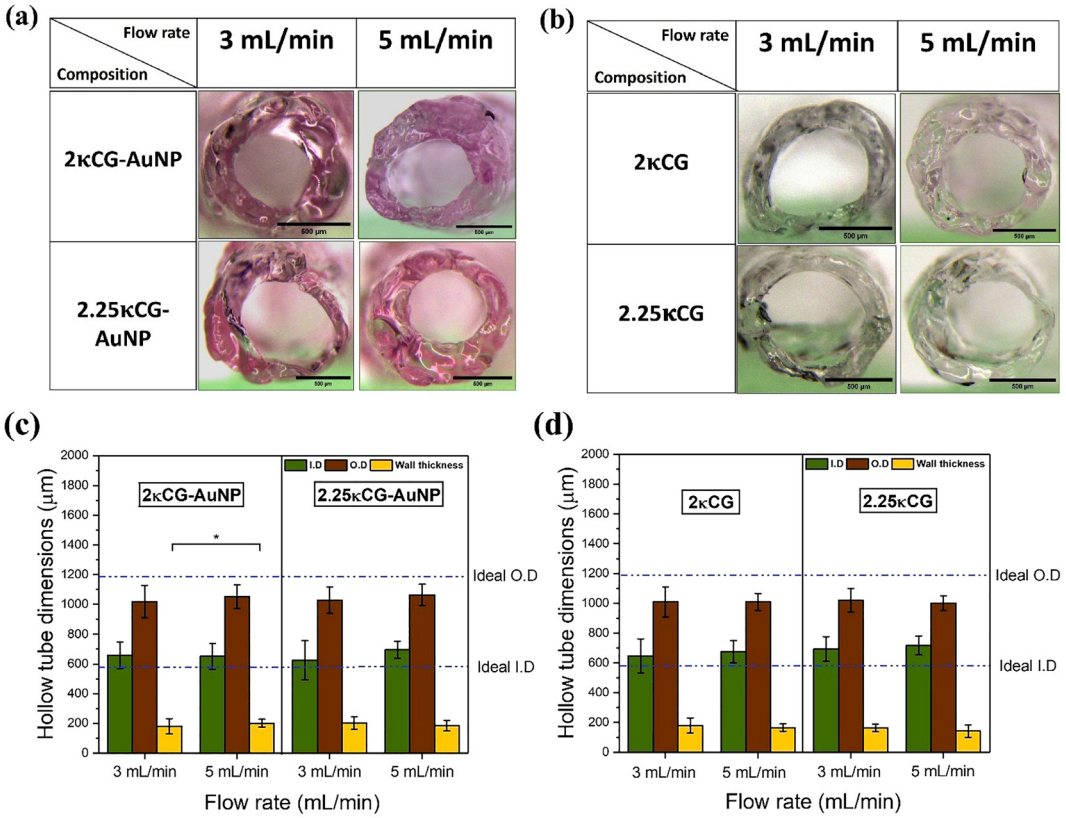

Fig. 4 Stereomicroscopic images of cross-sections of coaxially extruded hollow channels of varying compositions of (a) κCG–AuNPs; (b) pristine κCG (scale bar: 500 μm); (c) and (d) the effect of the flow rate of the sheath biopolymer on the I.D., O.D. and wall thickness of hollow channels of κCG–AuNP and pristine κCG hydrogels. One-way analysis of variance with Tukey's test was used for comparison, and $p < 0.05$ was considered to be statistically significant, indicated in the figure as '*' (n = 10 or n = 15).

Table 1 Average dimensions of ID, OD, wall thickness and circularity of pristine κCG and κCG–AuNP hollow conduits

Flow rate	3 mL min^{-1}				5 mL min^{-1}			
Composition	I.D. (μm)	O.D. (μm)	Wall thickness (μm)	Circularity	I.D. (μm)	O.D. (μm)	Wall thickness (μm)	Circularity
2κCG–AuNPs	658.2 ± 89.5	1018 ± 108.5	180.3 ± 51.1	0.88 ± 0.04	651 ± 86.1	1052.5 ± 78.9	200.7 ± 26.4	0.89 ± 0.06
2κCG	648.4 ± 114.3	1008.4 ± 101.2	180 ± 50.3	0.82 ± 0.09	676.5 ± 74.3	1008.3 ± 57.2	166.0 ± 25.0	0.87 ± 0.08
2.25κCG–AuNPs	625 ± 131.7	1028.3 ± 88.9	201.7 ± 42.2	0.85 ± 0.07	695.1 ± 58.5	1064.4 ± 71.5	184.7 ± 34.8	0.90 ± 0.03
2.25κCG	693.3 ± 83.7	1018 ± 79.3	162.4 ± 25.6	0.89 ± 0.06	718.1 ± 63.4	1000.3 ± 48.1	141.1 ± 41.3	0.92 ± 0.04

Fig. S5(a and b). The shear-thinning properties of the hydrogels at an extrusion temperature of 37 °C were demonstrated through flow curves. To assess the impact of the 100 mM KCl crosslinking bath used for post-extrusion crosslinking of hydrogel filaments, small amplitude oscillatory frequency sweeps were performed on both pristine κCG and κCG–AuNP hydrogel discs after incubation in the 100 mM KCl crosslinking bath.

3.4.1. Frequency sweeps of pristine κCG and κCG–AuNP hydrogels. All compositions demonstrated that the storage modulus (G') was greater than the loss modulus (G''), indicating an elastic gel-like behaviour throughout the measurement range of angular frequency, as shown in Fig. 6, panel (a) (i) and (ii). It was observed that as the weight percentage of κCG increased, the G' values for both pristine κCG and κCG–AuNP hydrogels also increased. 2.25κCG and 2.25κCG–AuNP hydrogels exhibited the highest G' and G'' values, respectively. Between the κCG and κCG–AuNP hydrogels, the κCG compositions showed higher G' values. Specifically, the G' values at 1 rad s^{-1} for the 1.5κCG–AuNP, 2κCG–AuNP, and 2.25κCG–AuNP hydrogels were 1.53, 1.96, and 1.64 times lower than those of the 1.5κCG, 2κCG, and 2.25κCG hydrogels, respectively, as depicted in Fig. 6, panel (a) (iii). Our findings align with those of prior reports written by Satish *et al.*, who synthesized gold nanospheres of size 11 ± 2 nm in carboxymethyl cellulose to prepare electroconductive bioinks suitable for bioprinting.[55] Upon assessment of the flow curves of the hydrogels, it was observed that the viscosity of pristine carboxymethyl cellulose was higher compared to that

Table 2 CV% of I.D., O.D., wall thickness and circularity of pristine κCG and κCG–AuNP hollow conduits

Flow rate	3 mL min^{-1}				5 mL min^{-1}			
Composition	I.D. CV%	O.D. CV%	Wall thickness CV%	Circularity CV%	I.D. CV%	O.D. CV%	Wall thickness CV%	Circularity CV%
2κCG–AuNPs	13.6	10.7	28.3	4.5	13.2	7.5	13.2	6.7
2κCG	17.6	10	28	11	11.0	5.7	15.1	9.2
2.25κCG–AuNPs	21.1	8.6	20.9	8.2	8.4	6.7	18.8	3.3
2.25κCG	12.1	7.8	15.8	6.7	8.8	4.8	29.3	4.3

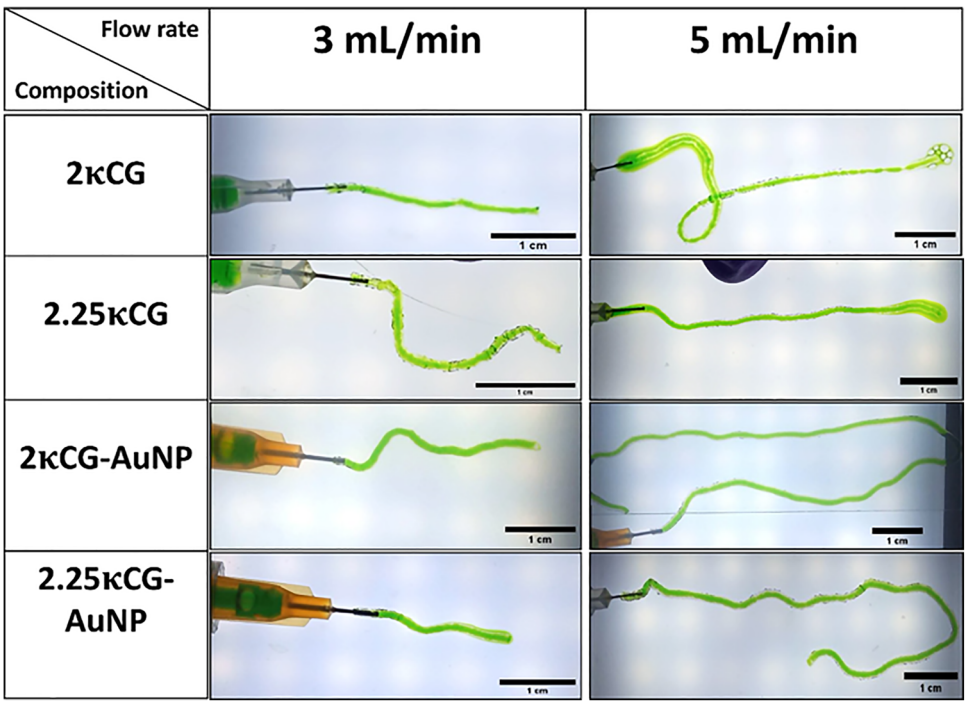

Fig. 5 Perfusion of food dye through the hollow lumens of tubular constructs of varying compositions of κCG and κCG–AuNPs coaxially extruded at different flow rates (scale bar: 1 cm).

of the *in situ* synthesized carboxymethyl cellulose. Similarly, the G' depicted in the LAOS and SAOS of the AuNP-containing hydrogel was significantly lower compared to that of the pristine hydrogel without altering the flow or viscoelastic properties of the hydrogels. The authors confirmed the reduction of Au ions by the hydroxyl (–OH) groups present in carboxymethyl cellulose, immobilising the gold nanospheres within the hydrogel matrices by XRD analysis. However, this phenomenon decreases interconnectivity between polymeric chains, leading to softer gels with lower G' and viscosity than the pristine hydrogels. Similarly, we believe that the hydroxyl groups in κCG reduced $HAuCl_4$ to Au^0, thereby stabilising the *in situ* synthesized AuNPs by acting as a capping agent. Due to the increased interaction of κCG polymeric chains with AuNPs, there is a reduction in hydrogen bond interaction between polymeric chains, as shown in FTIR results, resulting in the formation of softer gels with a reduction in G' compared to the pristine compositions. Additionally, the loss tangent ($\tan\delta$) of all samples ranges from 0.06 to 0.31, which suggests that they exhibit elastic solid-like behaviour. The loss tangent is defined as the ratio of G'' to G', as indicated in eqn (2) above. When $\tan\delta$ exceeds 1, it indicates liquid-like properties, whereas values below 1 correspond to a more solid-like behaviour.[56]

3.4.2. Flow curves of pristine κCG and κCG–AuNP hydrogels. As illustrated in Fig. 6, panel (b) (i) and (ii), the viscosity of both κCG–AuNP and κCG hydrogels exhibits a rapid decrease when the shear rates increase from 0.2 s^{-1} to 20 s^{-1}. Additionally, the low shear viscosity measured at 0.2 s^{-1} was found to be directly proportional to the weight percentage of κCG in both pristine κCG and κCG–AuNP hydrogels. Kim *et al.* previously demonstrated, using flow curves, that the viscosity of alginate–carrageenan composite hydrogels increases with higher concentrations of carrageenan, ranging from 0.5% (w/v) to 1.5% (w/v), when crosslinked with a fixed concentration of $CaSO_4$.[57] The shear-thinning properties were further quantified by fitting the power law mathematical model according to eqn (3). Fig. S6 shows the model fits of the flow curve data for the 1.5κCG–AuNP and 1.5κCG hydrogels to

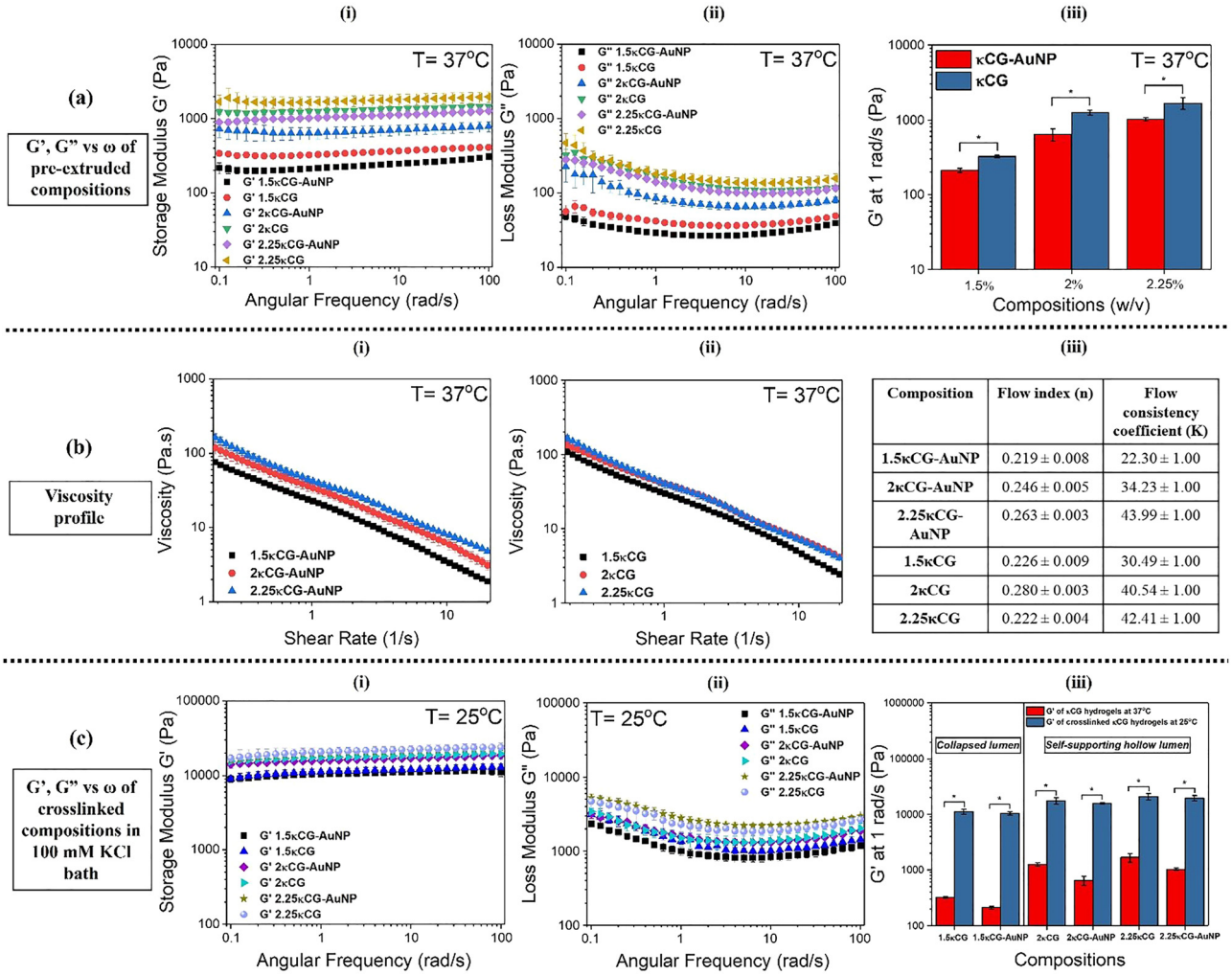

Composition	Flow index (n)	Flow consistency coefficient (K)
1.5κCG-AuNP	0.219 ± 0.008	22.30 ± 1.00
2κCG-AuNP	0.246 ± 0.005	34.23 ± 1.00
2.25κCG-AuNP	0.263 ± 0.003	43.99 ± 1.00
1.5κCG	0.226 ± 0.009	30.49 ± 1.00
2κCG	0.280 ± 0.003	40.54 ± 1.00
2.25κCG	0.222 ± 0.004	42.41 ± 1.00

Fig. 6 Panel (a) (i) frequency sweeps depicting the storage modulus (G') of varying compositions of pristine κCG and κCG–AuNPs, (ii) frequency sweeps depicting the loss modulus (G'') of varying compositions of pristine κCG and κCG–AuNPs, (iii) comparison of G' at 1 rad s^{-1} of varying compositions of pristine κCG and κCG–AuNPs; panel (b) flow curves showing the viscosity variation with the shear rate of varying compositions of (i) pristine κCG hydrogels; (ii) κCG–AuNP hydrogels, (iii) n and K table for all compositions of κCG–AuNP and pristine κCG hydrogels; panel (c) frequency sweeps of varying compositions of (i) κCG and (ii) κCG–AuNPs crosslinked in a 100 mM KCl bath, (iii) comparison of G' at 1 rad s^{-1} of varying compositions of pristine κCG and κCG–AuNPs at 37 °C before and after incubation in a 100 mM KCl crosslinking bath at 25 °C. One-way analysis of variance with Tukey's test was used for comparison, and $p < 0.05$ was considered statistically significant, indicated in the figure by '*' (n = 3).

estimate the parameters n and K. A shear-thinning fluid is characterized by having $n < 1$. Thus, from Fig. 6 panel b (iii), we can infer that all compositions of κCG hydrogels exhibit shear-thinning profiles with n values close to 0.2. The K values for both κCG–AuNP and κCG hydrogels increase with a higher weight percentage of κCG. Additionally, all compositions of κCG–AuNP hydrogels show lower K values compared to κCG hydrogels, indicating a reduction in viscosity due to the incorporation of AuNPs within the κCG hydrogel.

3.4.3. Frequency sweep of hydrogel inks crosslinked with a 100 mM KCl crosslinking bath. The large-amplitude oscillatory strain sweeps, which were conducted to determine the linear viscoelastic region (LVR), are shown in Fig. S5(c) and (d). After incubating 1.5κCG–AuNP hydrogels in the 100 mM KCl bath for half an hour, we observed a 49-fold increase in G' compared to G' measured at the extrusion temperature of 37 °C (Fig. 6, panel c (iii)). Similarly, for the 2κCG–AuNP and 2.25κCG–AuNP hydrogels, we noted a 25-fold and 19-fold increase in G', respectively.

For the 1.5κCG hydrogels, incubation in the 100 mM KCl solution resulted in a 34-fold increase in G' compared to the storage modulus at 37 °C. Similarly, for the 2κCG and 2.25κCG hydrogels, we observed a 14-fold and 12-fold increase in G', respectively, after incubation in the 100 mM KCl solution bath.

The increase in G' of κCG hydrogels after incubation in a 100 mM KCl crosslinking bath for 30 minutes is crucial for the formation of self-supporting hollow filaments upon removal of the sacrificial core. Although there were significant increases in G' – 34-fold for the 1.5κCG hydrogels and 49-fold for the 1.5κCG–AuNP hydrogels – both types of filaments exhibited

collapsed lumens and ruptured cross-sections (Fig. S4). Kim *et al.* reported that a 2.5% (w/v) alginate solution, crosslinked with 0.2% (w/v) $CaCl_2$ and yielding a G' of 500 Pa, is the optimal composition for producing filaments that are closest to a straight line without core leakage during coaxial printing.[58] Therefore, despite the increase in G' of both 1.5κCG–AuNP and 1.5κCG hydrogels to over 1000 Pa after extrusion in the crosslinking bath, their relatively low G' values of 211 Pa and 324 Pa, respectively, at the extrusion temperature of 37 °C may contribute to the collapse and rupture of the filaments after they are deposited in the crosslinking bath.

The linear viscoelastic regimes of all hydrogels at an extrusion temperature of 37 °C, along with the κCG hydrogels, after incubation in a crosslinking bath, were characterized through large amplitude oscillatory strain sweep tests (Fig. S5). No changes in moduli were observed at low-amplitude strains; however, as the strain increased, a decline in G' indicated deformation of the hydrogel. The point at which G' and G'' intersect is referred to as the critical strain, beyond which G'' dominates G', indicating liquid-like behaviour (Fig. S7(a)). It is evident from Fig. S7(b) that the bath-crosslinked hydrogels display a decrease in the critical strain compared to the hydrogels, regardless of the weight percentage of κCG or the presence of AuNPs. As demonstrated in Fig. S7(b), the critical strain of the 1.5κCG–AuNP hydrogel is 83.5%, compared to just 0.65% for the bath-crosslinked 1.5κCG–AuNP hydrogel. Similarly, 2κCG–AuNP and 2.25κCG–AuNP hydrogels showed reductions in critical strain from 49.7% and 14.4% to 0.56% and 0.47%, respectively, in the post-extrusion bath-crosslinked hydrogels. The compositions of 1.5κCG, 2κCG, and 2.25κCG hydrogels also show a decrease in critical strain from 44.2% to 0.55%, from 30.9% to 0.63%, and from 17.9% to 0.58%, respectively.

3.5. Mechanical characterization

The compressive moduli, load at failure and strain at failure of κCG and κCG–AuNP hydrogels before and after crosslinking in the 100 mM KCl bath are presented in Fig. 7. Fig. S8 shows the model fit of the linear region of the stress–strain plot for 2κCG–AuNP hydrogels.

A statistically significant increase in the compressive modulus of the 2κCG hydrogel was observed after incubation in the 100 mM KCl bath. Although no statistical differences were obtained for the rest of the compositions, the average compressive modulus values of the bath-crosslinked hydrogels were consistently higher than those of the same compositions not incubated in the 100 mM KCl bath. Fig. 7(b) denotes the maximum load the hydrogels can sustain until failure, which also complies with a significant increase upon crosslinking in a 100 mM KCl bath for all the compositions. Furthermore, Fig. 7(c) shows an increasing trend in the average maximum strain at failure after bath-crosslinking; however, statistical

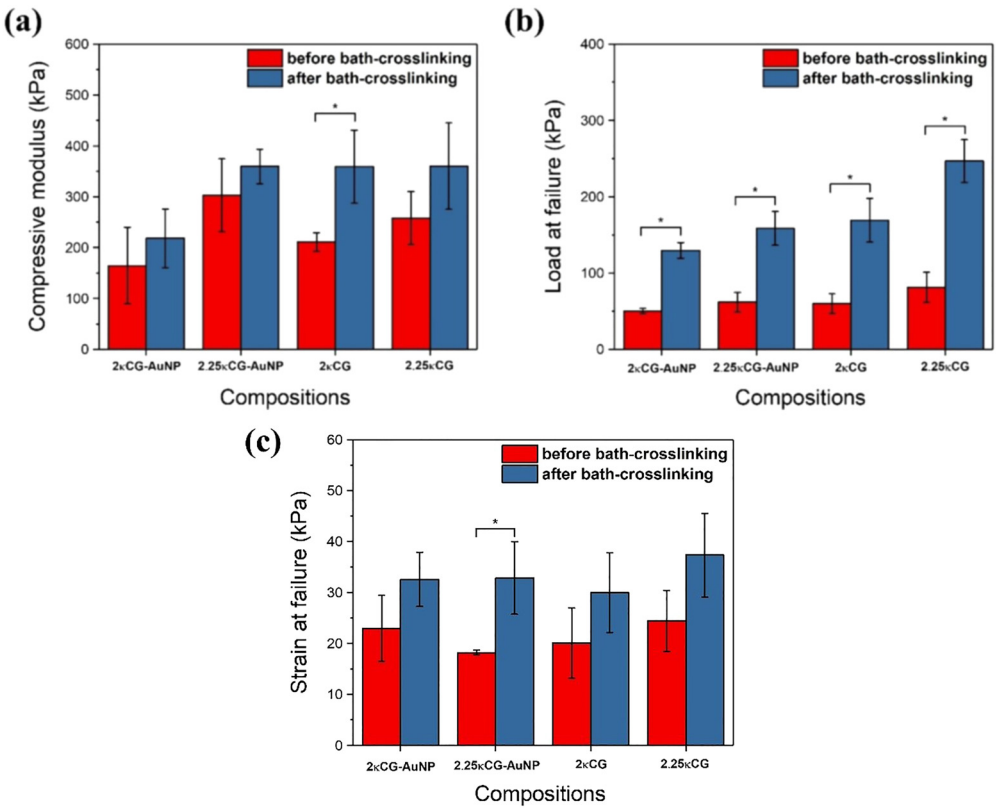

Fig. 7 Mechanical performance of varying compositions of κCG and κCG–AuNP hydrogels before and after crosslinking in a 100 mM KCl bath, (a) compressive moduli, (b) maximum load capacity before failure, and (c) maximum strain before failure. One-way analysis of variance with Tukey's test was used for comparison, and $p < 0.05$ was considered statistically significant, indicated in the figure by '*' ($n = 3$).

significance was observed only for 2.25κCG–AuNPs before and after crosslinking in 100 mM KCl.

Notably, all the hydrogels depicted a compressive modulus ranging between 165 and 303 kPa before incubation in the crosslinking bath and 218–360 kPa after incubation in the crosslinking bath, which are sufficiently higher compared to the compressive moduli of alginate-based hydrogels, previously used for bioprinting of perfusable constructs (34.5–50.7 kPa) and vascular tubes (6.58–8.38 kPa).[59,60] The above results indicate the critical role of the 100 mM KCl crosslinking bath in improving the mechanical properties of the hydrogels, which ensure the stability of the perfusable hollow channels after extrusion.

3.6. Pinch-off dynamics of hydrogel filaments

The filament-thinning behaviour over time was observed in all κCG and κCG–AuNP hydrogels. To illustrate this, Fig. 8 presents a sequence of images showing the filament thinning of κCG–AuNP hydrogels at a flow rate of 5 mL min^{-1}. A notable difference in filament pinch-off is evident when comparing the 2κCG–AuNP hydrogels with the other two types. The 2.25κCG–AuNP and 1.5κCG–AuNP hydrogels exhibited less elongation before pinch-off. In contrast, the 2κCG–AuNP sample exhibited a longer filament-thinning process, during which the filament elongated into a thinner thread just before pinch-off.

The image sequences have been quantified, and the plots are displayed in Fig. 9(a) and (b). Except for the 1.5κCG and 1.5κCG–AuNP hydrogels, where no filaments are formed, we observe that the presence of AuNPs increases the breakage or pinch-off time of filaments at both the 3 mL min^{-1} and 5 mL min^{-1} extrusion rates. The 2κCG–AuNP hydrogels exhibit the longest filament breakage time at the 5 mL min^{-1} extrusion rate. This finding aligns with our observations during the perfusion tests presented in Fig. 5. Previous studies on other biopolymers, such as xanthan gum, scleroglucan hydrogels, and nanocomposite solutions, have also examined pinch-off dynamics to investigate filament breakage time as a function of the biopolymer solutions and hydrogels' composition.[61,62]

In Table 3, we summarise the extensional relaxation time (λ) calculated from the exponential region of Fig. 9(a) and (b). This calculation was performed by fitting eqn (4), as shown in Fig. S9. The 2κCG–AuNP hydrogel filaments extruded at a flow rate of 5 mL min^{-1} exhibit the highest extensional relaxation time. This indicates that the material takes longer to relax its stress under extensional deformation, demonstrating significant resistance to stretching and behaving more like a solid.[32] This solid-like behaviour can be due to the role of AuNPs promoting molecular alignment under uniaxial tension. While this mechanism has not been widely explored, our findings suggest that nanoparticle–polymer interactions can critically influence filament thinning dynamics. Particularly in 2κCG–AuNPs, there may be an optimal balance of polymer–nanoparticle interactions, enabling better chain alignment and elastic recoil under uniaxial tension, giving slow filament breakup

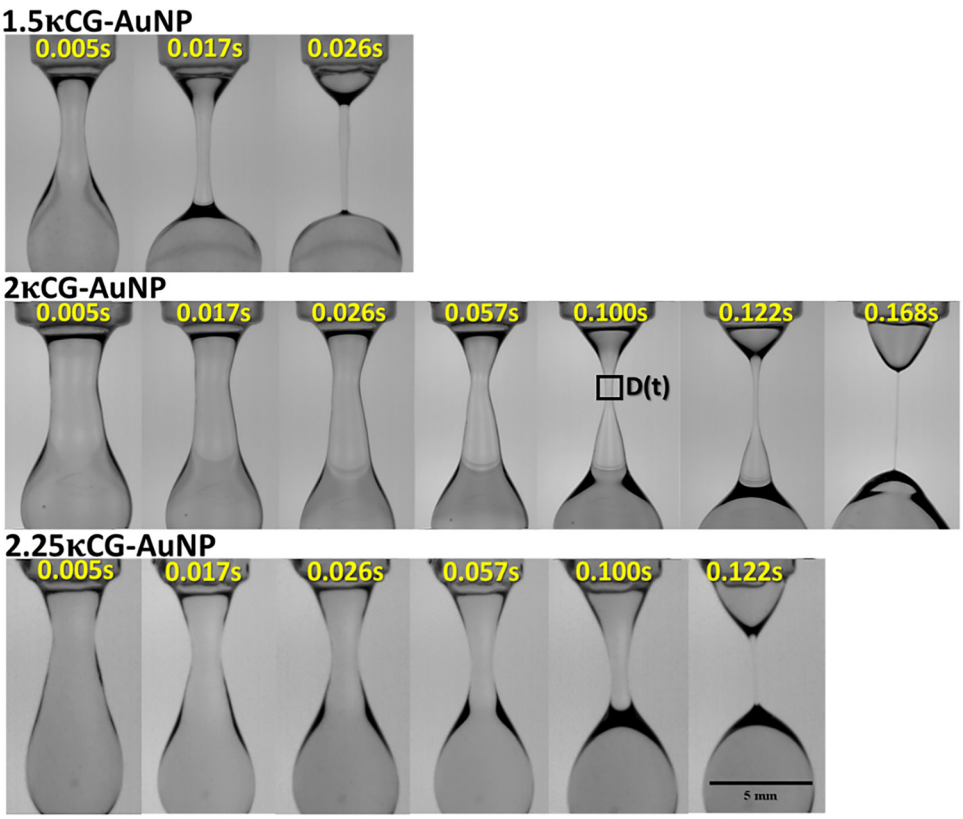

Fig. 8 κCG–AuNP hydrogel filament diameter thinning by dripping onto a substrate at a flow rate of 5 mL min^{-1} (scale bar: 5 mm).

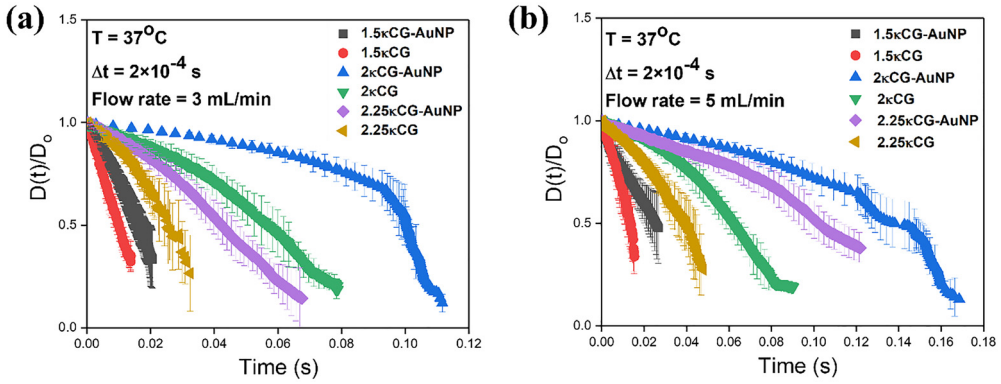

Fig. 9 Diameter evolution over time plotted for all compositions of κCG and κCG–AuNPs at a (a) 3 mL min^{-1} flow rate and (b) 5 mL min^{-1} flow rate.

Table 3 Extensional relaxation time (λ) of κCG and κCG–AuNP hydrogels

Composition	Surface tension (mN m^{-1})	Relaxation time λ (s)	
		3 mL min^{-1}	5 mL min^{-1}
1.5κCG–AuNPs	69.11 ± 2.2	0.0130 ± 0.001	0.0121 ± 0.001
1.5κCG	62.89 ± 2.4	0.007 ± 0.001	0.008 ± 0.001
2κCG–AuNPs	67.20 ± 3.2	0.113 ± 0.003	0.116 ± 0.002
2κCG	64.49 ± 1.7	0.046 ± 0.001	0.055 ± 0.003
2.25κCG–AuNPs	68.20 ± 2.7	0.032 ± 0.002	0.078 ± 0.002
2.25κCG	66.69 ± 1.9	0.021 ± 0.001	0.026 ± 0.001

under extension, leading to improved relaxation times, even though it is a softer gel (lower G'). Although 2.25κCG–AuNP exhibits higher G', it shows shorter pinch-off times and reduced filament elongation compared to 2κCG–AuNPs. This reflects that extrusion-driven filament stability is governed by a balance between stiffness and extensional viscoelasticity rather than by G' alone. A longer extensional relaxation time λ indicates that elastic stresses persist during necking and can markedly delay capillary breakup, yielding longer and thinner threads prior to pinch off. 2κCG–AuNPs may combine sufficient shear stiffness with the highest λ, suggesting an optimally stretchable, elastically dominated network under uniaxial extension. In contrast, 2.25κCG–AuNP likely possesses a more constrained network in which excess polymer limits chain alignment and elastic recoil, lowering effective extensional elasticity even though G' is higher. Thus, for coaxial extrusion of hollow filaments, the softer 2κCG–AuNP composition provides superior filament stability because its extensional response is better matched to the demands of the pinch off process than that of the stiffer 2.25κCG–AuNP.

Although limited literature directly addresses this behaviour in nanocomposite hydrogels, studies on entangled polymer solutions demonstrate that extensional relaxation time ratios decrease with increasing polymer concentration despite rise in G'.[63] Also, other unrelated systems, such as protein fibrils and polysaccharide solutions, have shown that extensional rheology reveals microstructural effects not evident in shear rheology.[64,65]

Fig. 10 illustrates the relationship between the extensional rate and extensional viscosity, as calculated from eqn (6) and (7). A similar trend, where extensional viscosity decreases with increasing extensional rate, has been documented using the filament stretching method.[66] This phenomenon, characterized by reduced resistance to deformation during stretching, is known as tension-thinning behaviour or extension thinning.[41,43,67] The overlapping curves observed at initial extensional rates across all compositions, regardless of κCG

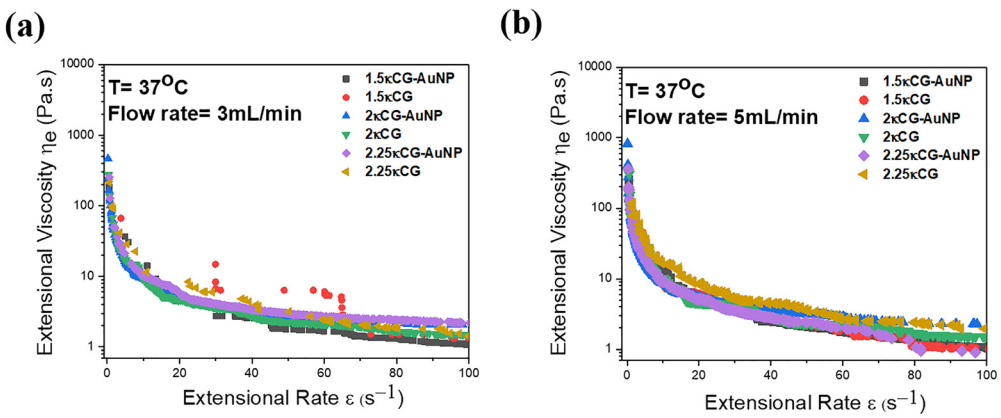

Fig. 10 Extensional viscosity *versus* extensional rate of κCG and κCG–AuNP hydrogels at a (a) 3 mL min^{-1} flow rate and (b) 5 mL min^{-1} flow rate.

concentration or the presence of AuNPs, suggest that the uncoiling and stretching of κCG occur similarly in each case.

Perfusion assays, rotational rheological studies, and pinch-off dynamics indicated that among all hydrogel formulations, the 2κCG–AuNP hydrogel extruded at a rate of 5 mL min^{-1} successfully formed self-supporting hollow filaments. These filaments exhibited resistance to breakage during manual handling, which can be attributed to a sufficiently high initial G' that increased further after crosslinking in a 100 mM KCl bath, highlighting their predominantly elastic properties. Therefore, we chose to encapsulate A549 lung carcinoma cells within 2κCG–AuNP hydrogels to create cell-laden hollow filaments using coaxial extrusion at the selected flow rate of 5 mL min^{-1}.

3.7. Rheological characterization of cell-laden hydrogels

Before assessing the cell viability of encapsulated A549 lung carcinoma cells in 2κCG–AuNP and 2κCG filaments following coaxial extrusion, we first examined how cell encapsulation affected the rotational and pinch-off dynamics of the 2κCG–AuNP and 2κCG hydrogels. The results from large amplitude oscillatory strain sweeps and small amplitude oscillatory frequency sweeps for both cell-laden and acellular compositions indicated that the addition of 2×10^6 cells per mL of A549 lung carcinoma cells led to a slight decrease in G' for both cell-laden 2κCG and 2κCG–AuNP hydrogels when compared with their acellular controls (Fig. 11). The flow curves denoted an increase in viscosity at lower shear rates for the cell laden 2κCG and 2κCG–AuNP hydrogels compared to the acellular gels.

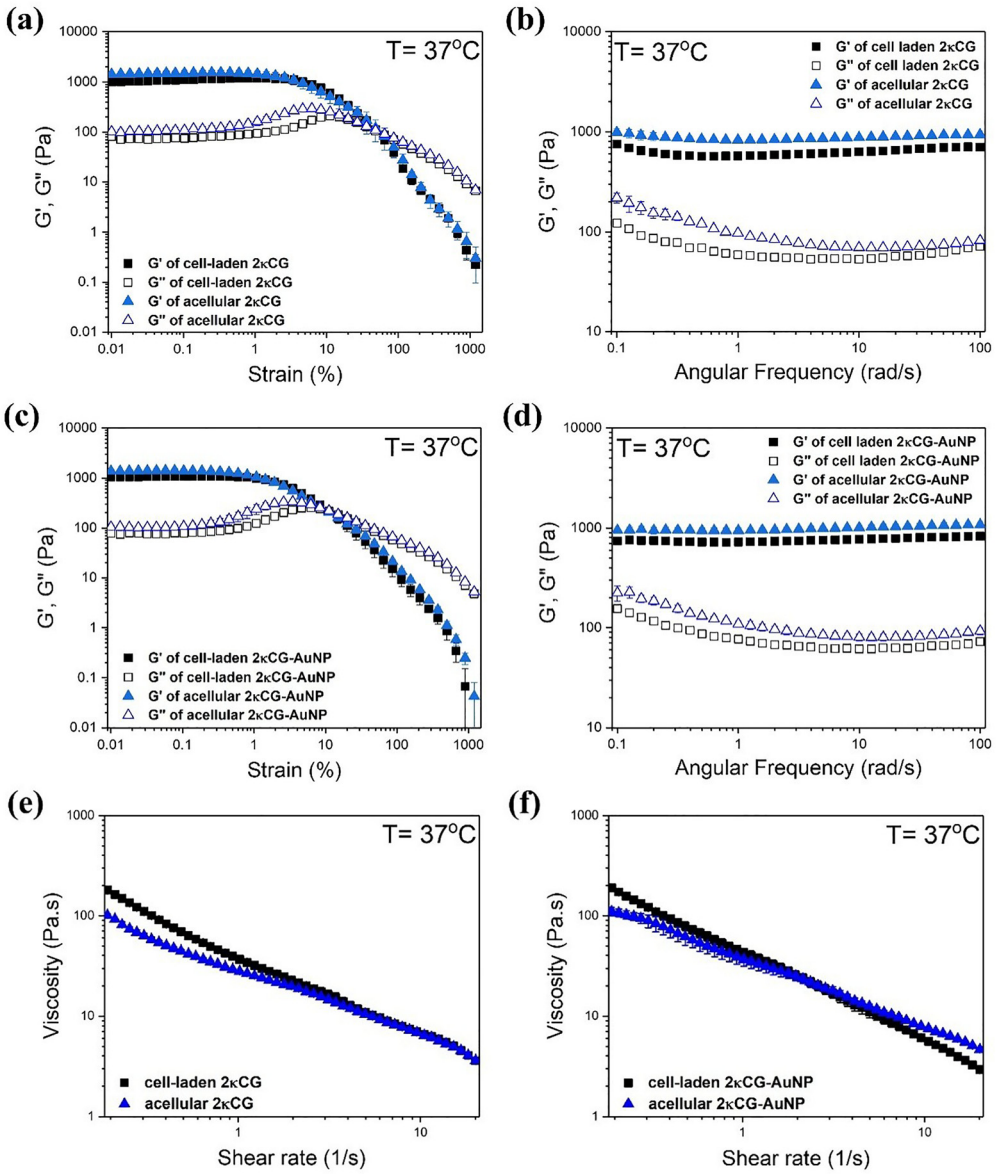

Fig. 11 (a and c) Comparison of large amplitude oscillatory strain sweeps of A549 encapsulated and acellular compositions of pristine 2κCG and 2κCG–AuNP hydrogels; (b and d) comparison of frequency sweeps of A549 encapsulated and acellular compositions of pristine 2κCG and 2κCG–AuNP hydrogels; (e and f) comparison of flow curves of A549 encapsulated and acellular compositions of pristine 2κCG and 2κCG–AuNP hydrogels.

The filament diameter decay obtained for A549 encapsulated and acellular 2κCG hydrogels and 2κCG–AuNP hydrogels from the pinch-off dynamics experiments (Fig. S10) showed a similar trend, except towards the end of the breakage process. The calculated extensional relaxation times (as shown in Table S3) for cell-encapsulated 2κCG and 2κCG–AuNP hydrogels, as well as for the acellular 2κCG and 2κCG–AuNP hydrogels, were not significantly different.

Diamantides *et al.* investigated the effect of chondrocyte inclusion on the rheological properties of collagen-based bioinks at very high cell densities ranging between 5×10^6 and 100×10^6 cells per mL, corresponding to a cell volume fraction of 0–0.18.[68] In their study, an increasing cell density led to a decrease in collagen G'. Although the cell volume fraction of the A549 lung carcinoma cells at a cell density of 2×10^6 cells per mL in 2κCG and 2κCG–AuNP hydrogels, in our study, is low (approximately 0.0061) compared to those reported by Diamantides *et al.*, we observed a small decrease in G' and an increase in viscosity at low shear compared to acellular gels. At this low cell volume fraction, the encapsulated cells may be acting as soft inclusions, disrupting the polymeric network and thereby slightly lowering the G' while increasing hydrodynamic resistance under steady shear. Similarly, Zhang *et al.* reported that the incorporation of cells into alginate-based inks led to an increase in shear viscosity alongside no significant changes in G'.[69]

3.8. Cell viability

As shown in Fig. 12, A549 cells were successfully encapsulated in 2κCG and 2κCG–AuNP compositions at a cell density of 2×10^6 cells per mL. The images in Fig. 12(a and b) clearly illustrate the cell-encapsulated walls and the hollow channels of the extruded filaments. Fig. S11 presents the 3D z-stacks depicting the uniform distribution of A549 cells throughout the conduit walls of 2κCG and 2κCG–AuNP hydrogels. The confocal z-stacks of 2κCG and 2κCG–AuNP hollow conduits were divided into four equal regions based on the total number of slices, and live and dead cells were quantified in each region (Tables S4 and S5). Each z-stack region indicates a sequential segment of the conduit wall along the imaging depth. The absence of any monotonic gradient in Table S4 in total cell number or viability along the *z*-axis indicates homogeneous encapsulation and no significant cell settling during the extrusion process. In Table S5, although a decrease in total cell number is observed with increasing imaging depth, gravitational settling should have resulted in higher cell numbers at the bottom, which was not observed. Moreover, the uniform cell viability across all regions (75–80%) indicates no depth-dependent cytotoxicity in the 2κCG–AuNP hollow conduit.

Upon encapsulation in both the 2κCG and 2κCG–AuNP hydrogels, the cells assumed a rounded morphology with a uniform distribution throughout the filament walls. This could be because of the lack of adhesion of A549 to the biopolymer chains due to the absence of adhesion sites in κCG polysaccharide.[70]

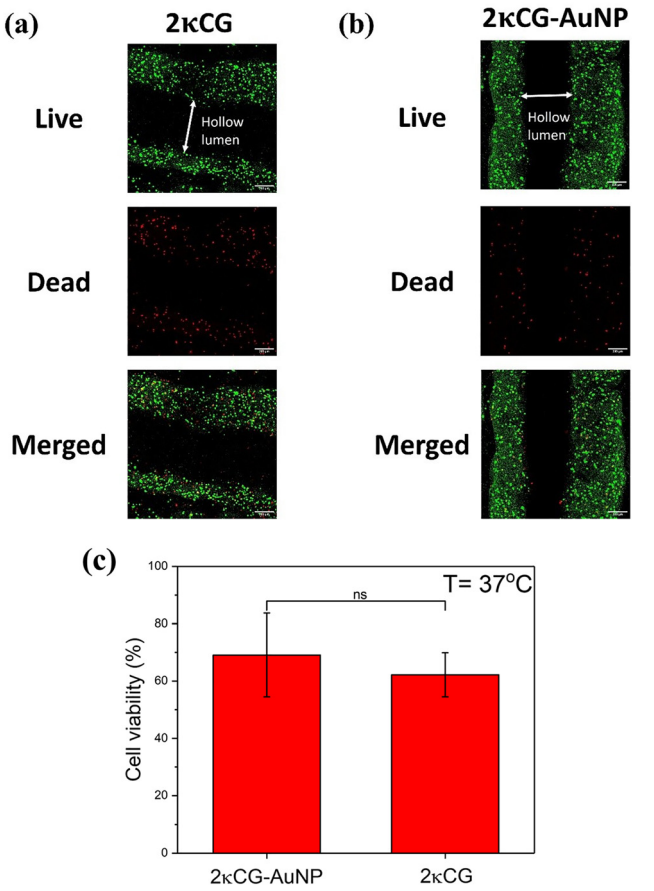

Fig. 12 (a and b) Maximum intensity projection of z-stacks of encapsulated A549 lung carcinoma cells in the walls of filaments of 2κCG and 2κCG–AuNP hydrogels, respectively, along with the presence of hollow channels; (c) cell viability after 24 hours of extrusion at a flow rate of 5 mL min^{-1}.

To quantitatively assess cell survival following the coaxial extrusion process and exposure to a 100 mM KCl crosslinking bath for 24 hours, a live/dead staining procedure was performed. The cell viability observed in the hollow conduits of 2κCG hydrogels was 62.2 ± 7%, while the viability in 2κCG–AuNP hydrogel hollow conduits was 69.2 ± 14.6%.

The G' of both 2κCG and 2κCG–AuNP (~1 kPa) aligned with the G' of healthy porcine lung tissue, thereby ensuring the fabrication of physiologically relevant *in vitro* models.[71] Based on the above literature, to further study the biocompatibility of these cells in a complete 3D microenvironment, we decided to encapsulate A549 cells completely in the reported hydrogel compositions to evaluate their viability in a more complex shape that requires multimaterial extrusion using a simple setup. Since the current study focusses on material and process optimisation and initial biocompatibility, the choice of bulk encapsulation of cells also aligns with our goals to assess cell survival and material–cell interaction after extrusion.

Fig. 12(c) indicates that the presence of AuNPs within the κCG polymer did not confer additional toxicity to the encapsulated A549 cells. To isolate the effect of the crosslinking agent, we conducted 2D control experiments by exposing A549 cells to

Table 4 Comparison of hydrogels reported in the current study with previously investigated biopolymers

Sheath biopolymer	Core	Crosslinking bath	Coaxial nozzle size	Type of extrusion	Flow rate range/pressure on sheath biopolymers	Outer diameter (μm)	Inner diameter (μm)	Wall thickness (μm)	G' (Pa)/ viscosity (Pa s)	Cell viability after 24 hours	Ref.
Alginate	$CaCl_2$	—	14G–18G	Syringe pump	0.5–2 mL min^{-1}	950–1400	600–1000	100–200	—	—	82
	$CaCl_2$	$CaCl_2$	18G–30G	Syringe pump	200–500 μL min^{-1}	1500–2000	250	~625	—	95% (cell seeded in hollow lumen)	83
	$CaCl_2$	$CaCl_2$	16G–21G	Syringe pump	0.5–1.5 mL min^{-1}	1000–1300	600 –1000	~150–200	—	92.9 ± 2.4% (encapsulated cells)	6
	PVA	—	25.8 mm L × 4.0 mm outer diameter	Centra Printhead of RX1 bioprinter	15–250 mbar	—	~400	~45–80	—	~75% (encapsulated cells)	84
	Pluronic F-127	Pluronic F-127	5G–9G	T&R Biofab Bioprinter	120–160 kPa	3121 ± 80–2948 ± 54	—	339 ± 41–976 ± 25	40/10	HUVECs seeded in lumen	85
	Cell suspension	$CaCl_2$	16G–21G	Syringe pump	15–30 mL h^{-1}	870.87 ± 17.96–886.71 ± 9.83	242.89 ± 14.76–527.49 ± 13.36	313–179.61	—	96.36 ± 1.54% (cells seeded in lumen)	86
SilkMA and GelMA	$CaCl_2$	—	16G–22G	Syringe pump	0.5–1.5 mL min^{-1}	913 ± 14–1327 ± 17	741 ± 5–1077 ± 40	86–125	—	>80% (cell seeded in lumen)	87
GelMA	Gelatin	—	17G/25G, 17G/26G, 17G/27G	Bioprinter	0.2 mL min^{-1}	—	200–1000	—	—	>80% (encapsulated cells)	88
Pristine κCG and κCG–AuNPs	**Pluronic F127**	**KCl**	**16G–20G**	**Syringe pump and manual**	**3–5 mL min^{-1}**	**1000–2000**	**600–800**	**~200**	**1250/301, 639/262**	**62.2 ± 7%, 69.2 ± 14.6% (encapsulated cells)**	**This study**

10 mM KCl for 24 hours and to 100 mM KCl for 30 minutes at 4 °C, as used for the synthesis of κCG hydrogels and the fabrication of hollow conduits. No significant cell death was observed compared with 2D control cultures, indicating that the residual KCl had no ionic or osmotic effect on cell survival, as measured 24 hours after extrusion of the hollow conduits (Fig. S12). Although AuNPs are known to have low acute toxicity both *in vitro* and *in vivo*, their size, shape, capping agent, and cell line type play critical roles in determining their toxic effects. Small spherical AuNPs (1.2 nm–1.4 nm), regardless of surface chemistry, are known to induce apoptosis and necrosis in cells.[72] Conversely, AuNPs of different shapes, like rods or the larger-sized flower and prism-shaped AuNPs, are generally considered safer.[73] Based on the current literature, AuNPs ranging from 10 nm to 40 nm with specific surface modifications have been shown to maintain good cell viability. For example, AuNPs approximately 14 nm in size, green-synthesized at low concentrations of κCG, demonstrated no significant cytotoxicity towards lung cancer epithelial cells, A549.[30] Similarly, carboxymethyl cellulose-capped AuNPs of size 11 nm showed moderate cytotoxicity of <80% in L929 mouse fibroblast cells only at very high concentrations of gel seeding in well plates.[74] Furthermore, Zhang *et al.* synthesized AuNPs in chitin gels with sizes varying from 23 to 81 nm and an average size of 40 nm. The chitin nanogels were biocompatible with HepG2 cells, resulting in cell viability exceeding 100%.[75] On a similar note, we also prioritised the formation of AuNPs within the safe size range (10–35 nm) to ensure no additional cytotoxicity in the cell-laden hollow tubes, as *in vitro* models. In addition, the concentration of AuNPs synthesized within 2κCG–AuNPs was quantified by using ICP-OES following complete acid digestion of lyophilised scaffolds. The composition exhibited a gold concentration of 64.6 ppm (mg kg^{-1} of the hydrogel), confirming that the measured concentration falls within the reported biocompatible range for cell-laden scaffolds. Samadian *et al.* have previously demonstrated that AuNP loadings of 40–80 ppm did not induce any significant cytotoxicity in MG-63 cells cultured on poly(L-lactic acid (PLLA))-based hydrogel scaffolds.[76]

Irrespective of the lack of cytotoxicity by AuNPs, the overall cell viability of 62% and 69% for 2κCG and 2κCG–AuNP hydrogel hollow filaments, respectively, falls below the ~75–95% range reported in the literature (Table 4). However, it is critical to note that encapsulating cells in a hydrogel results in significant cell death prior to extrusion.[77–80] Additionally, the optimized flow rate of 5 mL min^{-1} to obtain continuous extrusion of longer filaments is higher compared to the flow rates reported in the literature. For example, Yu *et al.* demonstrated that, as dispensing pressure increased, cells encapsulated in alginate and bioprinted with a coaxial nozzle showed a reduction in viability from 68% to 40%.[81] Hence, the extrusion process also imposes detrimental effects on the cells due to the high shear rates. Future applications using sophisticated coaxial extrusion bioprinters could mitigate shear-related damage during extrusion. While A549 cells assumed a spherical morphology within the walls of the hydrogel hollow filaments due

to the lack of adhesion sites, studies suggest that encapsulated cells, like fibroblasts, have the inherent potential to self-organise into 3D spheroids within the κCG hydrogel over time.[16] Thus, extending the incubation period of encapsulated cells within κCG hollow hydrogel tubes may improve cell viability *via* cell migration and spheroid formation. In spite of the above limitations, the cell viability results conclusively show that κCG and its gold nanocomposite derivative have potential for the bioprinting of complex geometries in more sophisticated setups, laying the groundwork for the development of *in vitro* core–shell coculture models with potential applications in drug screening and disease modelling.

4. Comparison with the current literature

Table 4 summarises research from the past decade on the fabrication of hollow hydrogel conduits using syringe pumps and coaxial bioprinters. The dimensions of the hollow conduits, namely, inner diameter (I.D.), outer diameter (O.D.) and wall thickness of κCG hollow hydrogel tubes, were targeted based on a literature review of the commonly fabricated dimensions of hollow channels.

As shown in Table 4, alginate-based hollow hydrogel channels have been extensively studied for creating hollow structures with wall thicknesses ranging from over 600 μm to as thin as 45 μm. The rapid crosslinking of alginate by Ca^{2+} allows for immediate gelation upon contact, facilitating the formation of tubular structures with strong mechanical properties. Similarly, UV-crosslinkable GelMA, another biopolymer commonly examined for coaxial printing, requires UV exposure to initiate crosslinking and enhance the mechanical properties of hollow conduits. The existing literature on alginate and GelMA primarily focuses on seeding various cell types within the hollow lumen. This seeding process can occur either directly during coaxial printing through the core nozzle or after extrusion. Such methods allow for the assessment of cell viability, spreading, and proliferation on the inner walls of the lumen. This approach helps prevent cell death caused by shear stress during extrusion and reduces the toxicity resulting from crosslinking agents used in the biopolymer. However, a few studies, including one conducted by Yin *et al.*, have attempted to encapsulate cells within the sheath biopolymer itself. This method resulted in a lower cell viability of approximately 75% after three days of culture.[84] While many studies emphasize the lower viscosity of commonly used biopolymers as a desirable characteristic for easier fabrication of hollow conduits, the rheological properties of these materials have not been thoroughly investigated, as shown in Table 3. Moreover, the current literature on hollow conduits primarily focuses on either pure biopolymers or biopolymer blends. Although nanomaterials have been extensively studied for 3D bioprinting, the use of nanocomposite hydrogels in coaxial bioprinting and extrusion remains limited.[89,90]

We have successfully fabricated hollow lumens of κCG with dimensions comparable to those reported in the literature. Although some studies have achieved the fabrication of smaller I.D. values (~200 μm) by core–sheath extrusion, they are difficult to characterize for quantitative analysis and biological assays. For example, Homan *et al.* successfully fabricated tubules with diameters as low as 150 μm, but quantitative assays were conducted only on tubules with diameters ranging from 400 μm to 550 μm.[91] The dimensions we targeted enabled us to perform quantitative assays such as cell viability measurements, along with perfusion of a food dye through the lumen to determine uniform formation of hollow channels. These perfusable channels not only confirm the formation of uniform hollow lumens but also facilitate proper exchange of nutrients and metabolic wastes from cells.[92] Moreover, the hollow tube dimensions with outer diameters ranging between 1000 and 1030 μm and inner diameters of 625–700 μm, fabricated in our study, closely replicate the tubular geometry of small bronchioles in the lungs.[93] Therefore, the obtained size range reflects the microscale architecture of the terminal airways in the lung, making the constructs well-suited for use in lung tissue engineering, disease modelling, or drug screening.

5. Conclusions and future outlook

In this study, we investigated key parameters, including the flow rate and composition, for pristine κCG and κCG–AuNPs to assess their impact on the fabrication of hollow tubular conduits. Rheological analysis showed that a low G' (<500 Pa) led to the collapse of hollow lumens in both pristine 1.5κCG and 1.5κCG–AuNPs, whereas intact hollow lumens were observed at higher compositions. Perfusability assay and pinch-off dynamics further indicated that a higher flow rate of 5 mL min^{-1} resulted in longer filaments with better mechanical integrity for manual handling, especially for 2κCG–AuNPs. A significant number of cells survived the coaxial extrusion process in both pristine κCG and κCG–AuNP cell-laden hollow conduits. These findings highlight the importance of the investigated parameters in determining the optimal composition and extrusion conditions necessary for the formation of hollow channels with potential for scaling up to model *in vitro* biological tubular structures using more advanced coaxial setups. In addition to the above, future investigations could explore varying the concentration of chloroauric acid to study its effect on the size of *in situ* synthesized AuNPs, and consequently, on the extrusion behaviour and fidelity of hollow conduits. Further studies on the 3D encapsulation of A549 can include extended culture durations to evaluate long-term cellular behaviour and functional assays to assess tissue-specific functionality of the constructs.

Author contributions

Sanchari Swarupa: experiments, data collection, analysis, writing; Mata Subhashita: pinch-off dynamics experiments, data

collection, analysis, writing; Nikita Chauhan: SAXS experiments, analysis; Jitendra Bahadur: SAXS analysis, writing; Sharad Gupta: cell culture experiment supervision; Prachi Thareja: overall supervision, reviewing, funding acquisition, and project administration.

Conflicts of interest

The authors declare no competing financial interests or personal relationships that could have influenced the work reported in this article.

Data availability

The data supporting this article have been included as part of the supplementary information (SI). Supplementary information is available: Additional experimental data including hydrodynamic size distribution of AuNPs, FTIR, SAXS pattern and fitting parameters, cross-section of hollow conduits, rheological analyses, compressive modulus calculation, relaxation time measurements, diameter decay profiles, confocal z-stack images of hollow conduits, depth-wise cell distribution analyses and 2D control experiments. See DOI: https://doi.org/10.1039/d6ma00245e.

Acknowledgements

Prachi Thareja is thankful to ANRF, DST, Govt of India (Grant # CRG/2020/006088) for funding. The authors would like to thank the Central Instrumentation Facility at IIT Gandhinagar for providing the Confocal Laser Scanning Microscope and Atomic Force Microscope, Prof. Pranab Mohapatra (Department of Civil Engineering) for providing access to a high-speed camera (DST Project No. IMP/2018/001320). The funding from DST-FIST is also acknowledged. For help with writing, we asked Grammarly to respond to these AI prompts: prompts created by Grammarly – ''Improve it''. Some figures in this manuscript were created using BioRender.com.

References

1 Y. Tian, Z. Wang and L. Wang, Hollow fibers: from fabrication to applications., *Chem. Commun.*, 2021, **57**(73), 9166–9177.
2 A. Kjar, B. McFarland, K. Mecham, N. Harward and Y. Huang, Engineering of tissue constructs using coaxial bioprinting, *Bioact. Mater.*, 2021, **6**, 460–471.
3 A. M. Van Genderen, M. G. Valverde, P. E. Capendale, M. V. Kersten, E. S. Garví, C. C. L. Schuurmans, M. Ruelas, J. T. Soeiro, G. Tang, M. J. Janssen, J. Jansen, S. M. Mihăilă, T. Vermonden, Y. S. Zhang and R. Masereeuw, Coaxial printing of convoluted proximal tubule for kidney disease modeling, *Biofabrication*, 2022, **14**(4), 044102.
4 Z. Wang, C. Huang, H. Liu, Z. Shi, X. Han, S. Li, J. Huang, Z. Wang, Y. Yan and Z. Chen, Two-step method fabricating a 3D nerve cell model with brain-like mechanical properties and tunable porosity vascular structures via coaxial printing, *Colloids Surf., B*, 2023, **224**, 113202.
5 S. Li, H. Li, X. Shang, J. He and Y. Hu, Recent advances in 3D printing sacrificial templates for fabricating engineered vasculature, *MedComm – Biomater. Appl.*, 2023, **2**(3), e46.
6 Q. Gao, Y. He, J. Fu, A. Liu and L. Ma, Coaxial nozzle-assisted 3D bioprinting with built-in microchannels for nutrients delivery, *Biomaterials*, 2015, **61**, 203–215.
7 G. Falcone, M. Saviano, R. P. Aquino, P. Del Gaudio and P. Russo, Coaxial semi-solid extrusion and ionotropic alginate gelation: a successful duo for personalized floating formulations via 3D printing, *Carbohydr. Polym.*, 2021, **260**, 117791.
8 H. Xu, Y. Su, Z. Liao, Z. Liu, X. Huang, L. Zhao, R. Duan, Y. Hu, Y. Wei, X. Lian and D. Huang, Coaxial bioprinting vascular constructs: a review, *Eur. Polym. J.*, 2022, **179**, 111549.
9 F. Liu, G. Duan and H. Yang, Recent advances in exploiting carrageenans as a versatile functional material for promising biomedical applications, *Int. J. Biol. Macromol.*, 2023, **235**, 123787.
10 D. M. C. Marques, J. C. Silva, A. P. Serro, J. M. S. Cabral, P. Sanjuan-Alberte and F. C. Ferreira, 3D bioprinting of novel κ-carrageenan bioinks: an algae-derived polysaccharide, *Bioengineering*, 2022, **9**(3), 109.
11 P. Patel, K. Mujmer, V. K. Aswal, S. Gupta and P. Thareja, Structure, rheology, and 3D printing of salt-induced κ-carrageenan gels, *Mater. Today Commun.*, 2023, **35**, 105807.
12 P. Patel, P. Gangwar and P. Thareja, Preparation and rheology of titanium dioxide nanoparticles loaded κ-carrageenan hydrogel beads strengthened by mixed salts for multipollutant water remediation, *J. Vinyl Addit. Technol.*, 2023, **29**, 773–794.
13 P. Patel, M. E. Jinugu and P. Thareja, Rheology and extrusion printing of κ-carrageenan/olive oil emulsion gel tablets with varying surface area to volume ratios for release of vitamin C and curcumin, *Langmuir*, 2024, **40**, 16069–16084.
14 A.-M. Hermansson, E. Eriksson and E. Jordansson, Effects of potassium, sodium and calcium on the microstructure and rheological behaviour of kappa-carrageenan gels, *Carbohydr. Polym.*, 1991, **16**, 297–320.
15 B. T. Nguyen, T. Nicolai, L. Benyahia and C. Chassenieux, Synergistic effects of mixed salt on the gelation of κ-carrageenan, *Carbohydr. Polym.*, 2014, **112**, 10–15.
16 W. Lim, G. J. Kim, H. W. Kim, J. Lee, X. Zhang, M. G. Kang, J. W. Seo, J. M. Cha, H. J. Park, M. Y. Lee, S. R. Shin, S. Y. Shin and H. Bae, Kappa-carrageenan-based dual cross-linkable bioink for extrusion type bioprinting, *Polymers*, 2020, **12**, 1–15.
17 K. Loukelis, D. Papadogianni and M. Chatzinikolaidou, Kappa-carrageenan/chitosan/gelatin scaffolds enriched with potassium chloride for bone tissue engineering, *Int. J. Biol. Macromol.*, 2022, **209**, 1720–1730.
18 S. M. Mihaila, A. K. Gaharwar, R. L. Reis, A. P. Marques, M. E. Gomes and A. Khademhosseini, Photocrosslinkable

kappa-carrageenan hydrogels for tissue engineering applications, *Adv. Healthcare Mater.*, 2013, **2**, 895–907.
19 S. M. Selimoglu and M. Elibol, Alginate as an immobilization material for MAb production via encapsulated hybridoma cells., *Crit. Rev. Biotechnol.*, 2010, **30**(2), 145–159.
20 S. Raveendran, Y. Yoshida, T. Maekawa and D. S. Kumar, Pharmaceutically versatile sulfated polysaccharide based bionano platforms, *Nanomedicine*, 2013, **9**, 605–626.
21 H. Wan, Z. Liu, Q. He, D. Wei, S. Mahmud and H. Liu, Bioreduction (AuIII to Au0) and stabilization of gold nanocatalyst using Kappa carrageenan for degradation of azo dyes, *Int. J. Biol. Macromol.*, 2021, **176**, 282–290.
22 M. Zhu, X. Li, L. Ge, Y. Zi, M. Qi, Y. Li, D. Li and C. Mu, Green synthesis of κ-carrageenan@Ag submicron-particles with high aqueous stability, robust antibacterial activity and low cytotoxicity, *Mater. Sci. Eng., C*, 2020, **106**, 110185.
23 M. Yadid, R. Feiner and T. Dvir, Gold nanoparticle-integrated scaffolds for tissue engineering and regenerative medicine, *Nano Lett.*, 2019, **19**, 2198–2206.
24 S. Boularaoui, A. Shanti, M. Lanotte, S. Luo, S. Bawazir, S. Lee, N. Christoforou, K. A. Khan and C. Stefanini, Nanocomposite conductive bioinks based on low-concentration GelMA and MXene nanosheets/gold nanoparticles providing enhanced printability of functional skeletal muscle tissues, *ACS Biomater. Sci. Eng.*, 2021, **7**, 5810–5822.
25 P. Nezhad-Mokhtari, M. Akrami-Hasan-Kohal and M. Ghorbani, An injectable chitosan-based hydrogel scaffold containing gold nanoparticles for tissue engineering applications, *Int. J. Biol. Macromol.*, 2020, **154**, 198–205.
26 R. Chen, Q. Chen, D. Huo, Y. Ding, Y. Hu and X. Jiang, *In situ* formation of chitosan–gold hybrid hydrogel and its application for drug delivery, *Colloids Surf., B*, 2012, **97**, 132–137.
27 X. Chen, W. Han, X. Zhao, W. Tang and F. Wang, Epirubicin-loaded marine carrageenan oligosaccharide capped gold nanoparticle system for pH-triggered anticancer drug release, *Sci. Rep.*, 2019, **9**(1), 6754.
28 X. Chen, X. Zhao, Y. Gao, J. Yin, M. Bai and F. Wang, Green synthesis of gold nanoparticles using carrageenan oligosaccharide and their in vitro antitumor activity, *Mar. Drugs*, 2018, **16**(8), 277.
29 K. M. Zepon, M. S. Marques, A. W. Hansen, C. do A. F. Pucci, F. D. P. Morisso, A. L. Ziulkoski, J. H. O. do Nascimento, R. F. Magnago and L. A. Kanis, Polymer-based wafers containing in situ synthesized gold nanoparticles as a potential wound-dressing material, *Mater. Sci. Eng., C*, 2020, **109**, 110630.
30 N. González-Ballesteros, M. D. Torres, N. Flórez-Fernández, L. Diego-González, R. Simón-Vázquez, M. C. Rodríguez-Argüelles and H. Domínguez, Eco-friendly extraction of *Mastocarpus stellatus* carrageenan for the synthesis of gold nanoparticles with improved biological activity, *Int. J. Biol. Macromol.*, 2021, **183**, 1436–1449.
31 M. S. Marques, M. Zepon, J. M. Heckler, F. D. P. Morisso, M. M. da Silva Paula and L. A. Kanis, One-pot synthesis of gold nanoparticles embedded in polysaccharide-based hydrogel: physical–chemical characterization and feasibility for large-scale production, *Int. J. Biol. Macromol.*, 2019, **124**, 838–845.
32 G. H. McKinley and T. Sridhar, Filament-stretching rheometry of complex fluids, *Annu. Rev. Fluid Mech.*, 2002, **34**, 375–415.
33 S. L. Anna and G. H. McKinley, Elasto-capillary thinning and breakup of model elastic liquids, *J. Rheol.*, 2001, **45**, 115–138.
34 V. Tirtaatmadja, G. H. McKinley and J. J. Cooper-White, Drop formation and breakup of low viscosity elastic fluids: effects of molecular weight and concentration, *Phys. Fluids*, 2006, **18**(4), 043101.
35 J. Dinic, L. N. Jimenez and V. Sharma, Pinch-off dynamics and dripping-onto-substrate (DoS) rheometry of complex fluids, *Lab Chip*, 2017, **17**, 460–473.
36 P. Patel, K. Mujmer, V. K. Aswal, S. Gupta and P. Thareja, Structure, rheology, and 3D printing of salt-induced κ-carrageenan gels, *Mater. Today Commun.*, 2023, **35**, 105807.
37 S. Zou, J. Ye, Y. Wei and J. Xu, Characterization of 3D-bioprinted in vitro lung cancer models using RNA-sequencing techniques, *Bioengineering*, 2023, **10**(6), 667.
38 X. Wang, X. Zhang, X. Dai, X. Wang, X. Li, J. Diao and T. Xu, Tumor-like lung cancer model based on 3D bioprinting, *3 Biotech*, 2018, **8**(12), 501.
39 I. Cruz-Matías, D. Ayala, D. Hiller, S. Gutsch, M. Zacharias, S. Estradé and F. Peiró, Sphericity and roundness computation for particles using the extreme vertices model, *J. Comput. Sci.*, 2019, **30**, 28–40.
40 A. Daerr and A. Mogne, Pendent_Drop: an ImageJ plugin to measure the surface tension from an image of a pendent drop, *J. Open Res. Softw.*, 2016, **4**, 3.
41 B. Yuan, C. Ritzoulis and J. Chen, Extensional and shear rheology of okra polysaccharides in the presence of artificial saliva, *NPJ Sci. Food*, 2018, **2**, 20.
42 X. Liu, C. Zhu, H. Dong, B. Wang, R. Liu, N. Zhao, S. Li and J. Xu, Effect of microgel content on the shear and extensional rheology of polyacrylonitrile solution, *Colloid Polym. Sci.*, 2015, **293**, 587–596.
43 H. A. Barnes, J. F. Hutton and K. Walters, Extensional viscosity, in *An Introduction to Rheology*, Rheology Series, Elsevier, 1989, vol. 3, pp. 75–96.
44 T. H. Meen, J. K. Tsai, S. M. Chao, Y. C. Lin, T. C. Wu, T. Y. Chang, L. W. Ji, W. Water, W. R. Chen, I. T. Tang and C. J. Huang, Surface plasma resonant effect of gold nanoparticles on the photoelectrodes of dye-sensitized solar cells, *Nanoscale Res. Lett.*, 2013, **8**, 1–6.
45 R. Bellotti, G. B. Picotto and L. Ribotta, AFM measurements and tip characterization of nanoparticles with different shapes, *Nanomanuf. Metrol.*, 2022, **5**, 127–138.
46 P. Englebienne, A. Van Hoonacker and M. Verhas, *Spectroscopy*, IOS Press, 2003, pp. 255–273.
47 J. Turkevich, Colloidal gold. Part II, *Gold Bull.*, 1985, **18**, 125–131.
48 K. M. Zepon, I. Otsuka, C. Bouilhac, E. C. Muniz, V. Soldi and R. Borsali, Glyco-nanoparticles made from self-assembly of

maltoheptaose-*block*-poly(methyl methacrylate): micelle, reverse micelle, and encapsulation, *Biomacromolecules*, 2015, **16**, 2012–2024.

49 M. Álvarez-Viñas, N. González-Ballesteros, M. D. Torres, L. López-Hortas, C. Vanini, G. Domingo, M. C. Rodríguez-Argüelles and H. Domínguez, Efficient extraction of carrageenans from *Chondrus crispus* for the green synthesis of gold nanoparticles and formulation of printable hydrogels, *Int. J. Biol. Macromol.*, 2022, **206**, 553–566.

50 D. A. de Almeida, A. C. de Oliveira, R. S. Klein, E. G. Bonafé, M. J. Kipper, A. F. Martins and J. P. Monteiro, κ-Carrageenan-capped core–shell gold@silver nanoparticles: optical device for hydrogen peroxide detection, *Nano-Struct. Nano-Obj.*, 2022, **30**, 100861.

51 S. Ahmad, H. Alam and P. Thareja, 3D printing of hydrogels: a synergistic approach of rheology and computational fluid dynamics (CFD) modeling, *RSC Adv.*, 2025, **15**, 39369–39390.

52 I. Arockia Mary, S. Selvanayagam, S. Selvasekarapandian, S. R. Srikumar, T. Ponraj and V. Moniha, Lithium ion conducting membrane based on K-carrageenan complexed with lithium bromide and its electrochemical applications, *Ionics*, 2019, **25**, 5839–5855.

53 R. Attalla, C. Ling and P. Selvaganapathy, Fabrication and characterization of gels with integrated channels using 3D printing with microfluidic nozzle for tissue engineering applications, *Biomed. Microdevices*, 2016, **18**, 1–12.

54 S. W. Sawyer, K. Takeda, A. Alayoubi, E. Mirdamadi, A. Zidan, S. R. Bauer and H. Degheidy, 3D bioprinting optimization of human mesenchymal stromal cell laden gelatin-alginate-collagen bioink, *Biomed. Mater.*, 2023, **18**(1), 015016.

55 P. B. Sathish, S. Janani, P. Nithiya, S. Suriyaprakash and R. Selvakumar, Insitu synthesis of gold nanospheres immobilised carboxymethyl cellulose-based conductive hydrogel bioink for 3D bioprinting technology, *Mater. Lett.*, 2024, **359**, 135936, DOI: 10.1016/j.matlet.2024.135936.

56 A. A. Mohamed, S. Hussain, M. S. Alamri, A. A. Abdo Qasem, M. A. Ibraheem and M. I. Alhazmi, Dynamic rheological properties of corn starch-date syrup gels, *J. Food Sci. Technol.*, 2019, **56**, 927–936.

57 M. H. Kim, Y. W. Lee, W. K. Jung, J. Oh and S. Y. Nam, Enhanced rheological behaviors of alginate hydrogels with carrageenan for extrusion-based bioprinting, *J. Mech. Behav. Biomed. Mater.*, 2019, **98**, 187–194.

58 M. H. Kim and S. Y. Nam, Assessment of coaxial printability for extrusion-based bioprinting of alginate-based tubular constructs, *Bioprinting*, 2020, **20**, e00092.

59 W. Jia, P. S. Gungor-Ozkerim, Y. S. Zhang, K. Yue, K. Zhu, W. Liu, Q. Pi, B. Byambaa, M. R. Dokmeci, S. R. Shin and A. Khademhosseini, Direct 3D bioprinting of perfusable vascular constructs using a blend bioink, *Biomaterials*, 2016, **106**, 58–68.

60 M. Ye, B. Lu, X. Zhang, B. Li, Z. Xiong and T. Zhang, Coaxial embedded printing of gelatin methacryloyl–alginate double network hydrogel for multilayer vascular tubes, *Chin. J. Mech. Eng.: Addit. Manuf. Front.*, 2022, **1**, 100024.

61 X. Li, S. E. Harding, B. Wolf and G. E. Yakubov, Instrumental characterization of xanthan gum and scleroglucan solutions: comparison of rotational rheometry, capillary breakup extensional rheometry and soft-contact tribology, *Food Hydrocolloids*, 2022, **130**, 107681.

62 O. Akhlaghi, O. Akbulut and Y. Z. Menceloglu, Shear and extensional rheological characterization of poly(acrylonitrile)/halloysite nanocomposite solutions, *Eur. Polym. J.*, 2015, **73**, 17–25.

63 D. Sachsenheimer, B. Hochstein and N. Willenbacher, Experimental study on the capillary thinning of entangled polymer solutions, *Rheol. Acta*, 2014, **53**, 725–739.

64 Y. Zhao, C. Wang, Y. Chang, S. Li, C. Sun and Y. Fang, Environmental parameters-dependent rheological behaviors of whey protein fibril dispersions: shear and extensional flow behaviors, *Food Hydrocolloids*, 2022, **133**, 107974.

65 V. Evageliou, Shear and extensional rheology of selected polysaccharides, *Int. J. Food Sci. Technol.*, 2020, **55**, 1853–1861.

66 C. J. S. Petrie, Extensional viscosity: a critical discussion, *J. Nonnewton. Fluid Mech.*, 2006, **137**, 15–23.

67 L. Xu, M. Ju, W. Guo and S. Yu, Extensional Rheology of poly(vinylidene fluoride)/*N*,*N*-dimethylformamide solutions, *Polymers*, 2023, **15**, 1119.

68 N. Diamantides, C. Dugopolski, E. Blahut, S. Kennedy and L. J. Bonassar, High density cell seeding affects the rheology and printability of collagen bioinks, *Biofabrication*, 2019, **11**(4), 045016.

69 Z. Zhang, C. Xu, R. Xiong, D. B. Chrisey and Y. Huang, Effects of living cells on the bioink printability during laser printing, *Biomicrofluidics*, 2017, **11**(3), 034120.

70 D. Almeida, F. Küppers, A. Gusmão, A. C. Manjua, C. F. R. Ferreira, C. A. M. Portugal, J. C. Silva, P. Sanjuan-Alberte and F. C. Ferreira, Design of magnetic kappa-carrageenan-collagen bioinks for 3D bioprinting, *J. Mater. Sci.*, 2024, **59**, 14573–14592.

71 S. R. Polio, A. N. Kundu, C. E. Dougan, N. P. Birch, D. Ezra Aurian-Blajeni, J. D. Schiffman, A. J. Crosby and S. R. Peyton, Cross-platform mechanical characterization of lung tissue, *PLoS One*, 2018, **13**(10), e0204765.

72 Y. Pan, S. Neuss, A. Leifert, M. Fischler, F. Wen, U. Simon, G. Schmid, W. Brandau and W. Jahnen-Dechent, Size-dependent cytotoxicity of gold nanoparticles, *Small*, 2007, **3**, 1941–1949.

73 E. O. Mikhailova, Gold nanoparticles: biosynthesis and potential of biomedical application, *J. Funct. Biomater.*, 2021, **12**(4), 70.

74 P. B. Sathish, S. Janani, P. Nithiya, S. Suriyaprakash and R. Selvakumar, *In situ* synthesis of gold nanospheres immobilised carboxymethyl cellulose-based conductive hydrogel bioink for 3D bioprinting technology, *Mater. Lett.*, 2024, **359**, 135936.

75 J. Zhang, W. Zhu, J. Liang, L. Li, L. Zheng, X. Shi, C. Wang, Y. Dong, C. Li and X. Zhu, *In situ* synthesis of gold nanoparticles from chitin nanogels and their drug release response to stimulation, *Polymers*, 2024, **16**(3), 390.

76 H. Samadian, H. Khastar, A. Ehterami and M. Salehi, Bioengineered 3D nanocomposite based on gold nanoparticles and gelatin nanofibers for bone regeneration: *in vitro* and *in vivo* study, *Sci. Rep.*, 2021, **11**(1), 13877.

77 E. G. Popa, S. G. Caridade, J. F. Mano, R. L. Reis and M. E. Gomes, Chondrogenic potential of injectable κ-carrageenan hydrogel with encapsulated adipose stem cells for cartilage tissue-engineering applications, *J. Tissue Eng. Regen. Med.*, 2015, **9**, 550–563.

78 H. A. Awad, M. Quinn Wickham, H. A. Leddy, J. M. Gimble and F. Guilak, Chondrogenic differentiation of adipose-derived adult stem cells in agarose, alginate, and gelatin scaffolds, *Biomaterials*, 2004, **25**, 3211–3222.

79 E. Marsich, M. Borgogna, I. Donati, P. Mozetic, B. L. Strand, S. G. Salvador, F. Vittur and S. Paoletti, Alginate/lactose-modified chitosan hydrogels: a bioactive biomaterial for chondrocyte encapsulation, *J. Biomed. Mater. Res. A*, 2008, **84**, 364–376.

80 Y. Wei, Y. Hu, W. Hao, Y. Han, G. Meng, D. Zhang, Z. Wu and H. Wang, A novel injectable scaffold for cartilage tissue engineering using adipose-derived adult stem cells, *J. Orthop. Res.*, 2008, **26**, 27–33.

81 Y. Yu, Y. Zhang, J. A. Martin and I. T. Ozbolat, Evaluation of cell viability and functionality in vessel-like bioprintable cell-laden tubular channels, *J. Biomech. Eng.*, 2013, **135**(9), 091011.

82 J. Sun, Y. Gong, M. Xu, H. Chen, H. Shao and R. Zhou, Coaxial 3D bioprinting process research and performance tests on vascular scaffolds, *Micromachines*, 2024, **15**(4), 463.

83 A. M. van Genderen, M. G. Valverde, P. E. Capendale, M. V. Kersten, E. S. Garví, C. C. L. Schuurmans, M. Ruelas, J. T. Soeiro, G. Tang, M. J. Janssen, J. Jansen, S. M. Mihăilă, T. Vermonden, Y. S. Zhang and R. Masereeuw, Co-axial printing of convoluted proximal tubule for kidney disease modeling, *Biofabrication*, 2022, **14**, 044102.

84 Y. Yin, E. J. Vázquez-Rosado, D. Wu, V. Viswanathan, A. Farach, M. C. Farach-Carson and D. A. Harrington, Microfluidic coaxial 3D bioprinting of cell-laden microfibers and microtubes for salivary gland tissue engineering, *Biomater. Adv.*, 2023, **154**, 213588.

85 A. Ahmad, S. J. Kim, Y. J. Jeong, M. S. Khan, J. Park, D. W. Lee, C. Lee, Y. J. Choi and H. G. Yi, Coaxial bioprinting of a stentable and endothelialized human coronary artery-sized *in vitro* model, *J. Mater. Chem. B*, 2024, **12**(35), 8633–8646.

86 X. Dai, L. Liu, J. Ouyang, X. Li, X. Zhang, Q. Lan and T. Xu, Coaxial 3D bioprinting of self-assembled multicellular heterogeneous tumor fibers, *Sci. Rep.*, 2017, **7**, 1457.

87 Z. Wu, H. Cai, Z. Ao, J. Xu, S. Heaps and F. Guo, Microfluidic printing of tunable hollow microfibers for vascular tissue engineering, *Adv. Mater. Technol.*, 2021, **6**, e2000683.

88 L. Shao, Q. Gao, C. Xie, J. Fu, M. Xiang and Y. He, Directly coaxial 3D bioprinting of large-scale vascularized tissue constructs, *Biofabrication*, 2020, **12**(3), 035014.

89 S. A. Wilson, L. M. Cross, C. W. Peak and A. K. Gaharwar, Shear-Thinning and Thermo-Reversible Nanoengineered Inks for 3D Bioprinting, *ACS Appl. Mater. Interfaces*, 2017, **9**, 43449–43458.

90 S. G. Marapureddy, P. Hivare, A. Sharma, J. Chakraborty, S. Ghosh, S. Gupta and P. Thareja, Rheology and direct write printing of chitosan - graphene oxide nanocomposite hydrogels for differentiation of neuroblastoma cells, *Carbohydr. Polym.*, 2021, **269**, 118254.

91 K. A. Homan, D. B. Kolesky, M. A. Skylar-Scott, J. Herrmann, H. Obuobi, A. Moisan and J. A. Lewis, Bioprinting of 3D convoluted renal proximal tubules on perfusable chips, *Sci. Rep.*, 2016, **6**, 34845.

92 D. B. Kolesky, R. L. Truby, A. S. Gladman, T. A. Busbee, K. A. Homan and J. A. Lewis, 3D bioprinting of vascularized, heterogeneous cell-laden tissue constructs, *Adv. Mater.*, 2014, **26**, 3124–3130.

93 M. Barreiro Carpio, M. Dabaghi, J. Ungureanu, M. R. Kolb, J. A. Hirota and J. M. Moran-Mirabal, 3D bioprinting strategies, challenges, and opportunities to model the lung tissue microenvironment and its function, *Front. Bioeng. Biotechnol.*, 2021, **9**, 2021.